Article

Cell Reports

Enhancing Chemotherapy Efficacy in *Pten*-Deficient Prostate Tumors by Activating the Senescence-Associated Antitumor Immunity

Graphical Abstract

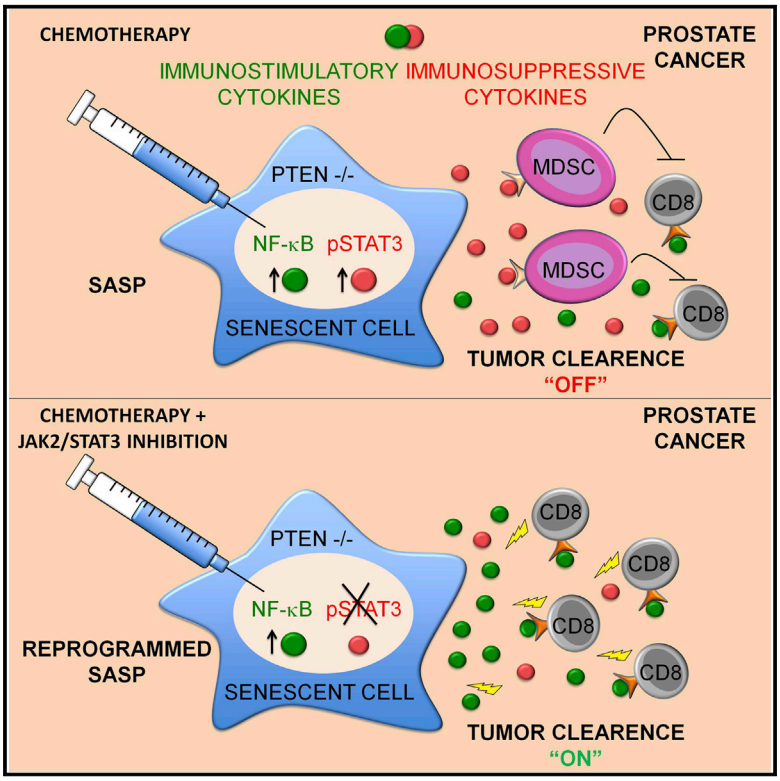

Highlights

Pten-loss-induced cellular senescence is characterized by an immunosuppressive SASP

SASP reprogramming restores senescence surveillance and tumor clearance

Senescent secretome reprogramming enhances chemotherapy efficacy

The senescent secretome depends on the genetic background of senescent tumor cells

Authors

Alberto Toso, Ajinkya Revandkar, ..., Carlo V. Catapano, Andrea Alimonti

Correspondence

andrea.alimonti@ior.iosi.ch

In Brief

Cytokines released by senescent cells can have pro- as well as antitumorigenic effects. Here, Toso et al. show that cytokines released by *Pten*-null senescent prostate tumors drive an immunosuppressive tumor microenvironment. Pharmacological inhibition of the Jak2/Stat3 pathway in *Pten*-deficient prostate tumors reprograms the senescence-associated cytokine network, leading to an antitumor immune response that enhances chemotherapy efficacy. These data demonstrate that immune surveillance of senescent tumor cells can be suppressed in specific genetic backgrounds but is also evoked by pharmacological treatments.

Toso et al., 2014, Cell Reports 9, 75–89
October 9, 2014 ©2014 The Authors
http://dx.doi.org/10.1016/j.celrep.2014.08.044

Cell Reports
Article

Enhancing Chemotherapy Efficacy in *Pten*-Deficient Prostate Tumors by Activating the Senescence-Associated Antitumor Immunity

Alberto Toso,[1] Ajinkya Revandkar,[1,8] Diletta Di Mitri,[1] Ilaria Guccini,[1] Michele Proietti,[2] Manuela Sarti,[1] Sandra Pinton,[1] Jiangwen Zhang,[3] Madhuri Kalathur,[1,8] Gianluca Civenni,[1] David Jarrossay,[2] Erica Montani,[2] Camilla Marini,[2] Ramon Garcia-Escudero,[1,6,9] Eugenio Scanziani,[4,5] Fabio Grassi,[2] Pier Paolo Pandolfi,[7] Carlo V. Catapano,[1] and Andrea Alimonti[1,8,*]

[1]Institute of Oncology Research (IOR) and Oncology Institute of Southern Switzerland (IOSI), Bellinzona 6500, Switzerland
[2]Institute for Research in Biomedicine (IRB), Bellinzona 6500, Switzerland
[3]Faculty of Arts and Sciences (FAS), Center for Systems Biology, Harvard University, Cambridge, MA 02138, USA
[4]Department of Animal Pathology, University of Milan, Milan 20139, Italy
[5]Mouse and Animal Pathology Laboratory, Fondazione Filarete, Milan 20139, Italy
[6]Molecular Oncology Unit, CIEMAT, Madrid 28040, Spain
[7]Cancer Genetics Program, Beth Israel Deaconess Cancer Center, Department of Medicine, Beth Israel Deaconess Medical Center, Harvard Medical School, Boston, MA 02215, USA
[8]Faculty of Biology and Medicine, University of Lausanne, UNIL, Rue du Bugnon 21, Lausanne 1011, Switzerland
[9]Oncogenomics Unit, Institute of Biomedical Research, Hospital "12 de Octubre", 28041 Madrid, Spain
*Correspondence: andrea.alimonti@ior.iosi.ch
http://dx.doi.org/10.1016/j.celrep.2014.08.044

SUMMARY

Prosenescence therapy has recently emerged as a novel therapeutic approach for treating cancer. However, this concept is challenged by conflicting evidence showing that the senescence-associated secretory phenotype (SASP) of senescent tumor cells can have pro- as well as antitumorigenic effects. Herein, we report that, in *Pten*-null senescent tumors, activation of the Jak2/Stat3 pathway establishes an immunosuppressive tumor microenvironment that contributes to tumor growth and chemoresistance. Activation of the Jak2/Stat3 pathway in *Pten*-null tumors is sustained by the downregulation of the protein tyrosine phosphatase PTPN11/SHP2, providing evidence for the existence of a novel PTEN/SHP2 axis. Importantly, treatment with docetaxel in combination with a JAK2 inhibitor reprograms the SASP and improves the efficacy of docetaxel-induced senescence by triggering a strong antitumor immune response in *Pten*-null tumors. Altogether, these data demonstrate that immune surveillance of senescent tumor cells can be suppressed in specific genetic backgrounds but also evoked by pharmacological treatments.

INTRODUCTION

Cellular senescence, an irreversible cell growth arrest involving the p53 and the p16INKA tumor suppressors, can be triggered by different insults including activation of oncogenes (oncogene-induced senescence [OIS]) or loss of tumor-suppressor genes (Braig et al., 2005; Chen et al., 2005; Collado, 2010). Over the past years, several in vivo evidences have demonstrated that senescence opposes tumor initiation and progression in different mouse models (Collado, 2010; Nardella et al., 2011). However, recent findings demonstrate that senescent tumor cells secrete a variety of immune modulators and inflammatory cytokines, referred to as the senescence-associated secretory phenotype (SASP), that mediate opposing and contradictory effects. The SASP can stimulate the innate and adaptive antitumor immune response (a process designated as "senescence surveillance"), leading to tumor clearance, but also promotes tumorigenesis by supporting the proliferation of neighboring tumor cells (Kang et al., 2011; Xue et al., 2007; Coppé et al., 2010; Rodier and Campisi, 2011; Davalos et al., 2010). Of note, the SASP can also hinder chemotherapy efficacy (Jackson et al., 2012). Therefore, the contradictory effects of the SASP cast doubts over the possibility to use treatments that enhance senescence for cancer therapy (Collado, 2010; Nardella et al., 2011). Moreover, whereas cytokines released by senescent tumors have been shown to positively regulate the antitumor immune response in some experimental models, it is unknown whether cytokines released by senescent tumors may also favor an immunosuppressive tumor microenvironment. An intriguing possibility is that the genetic background of senescent tumor cells may dictate the strength and composition of the cytokines released by the tumor, therefore impacting differently on the tumor microenvironment, specifically the immune system. We have previously demonstrated that *Pten*-loss-induced cellular senescence (PICS) is a novel type of cellular senescence response that occurs in vivo and that can be enhanced by pharmacological treatments (Alimonti et al., 2010). *Pten*-null prostate

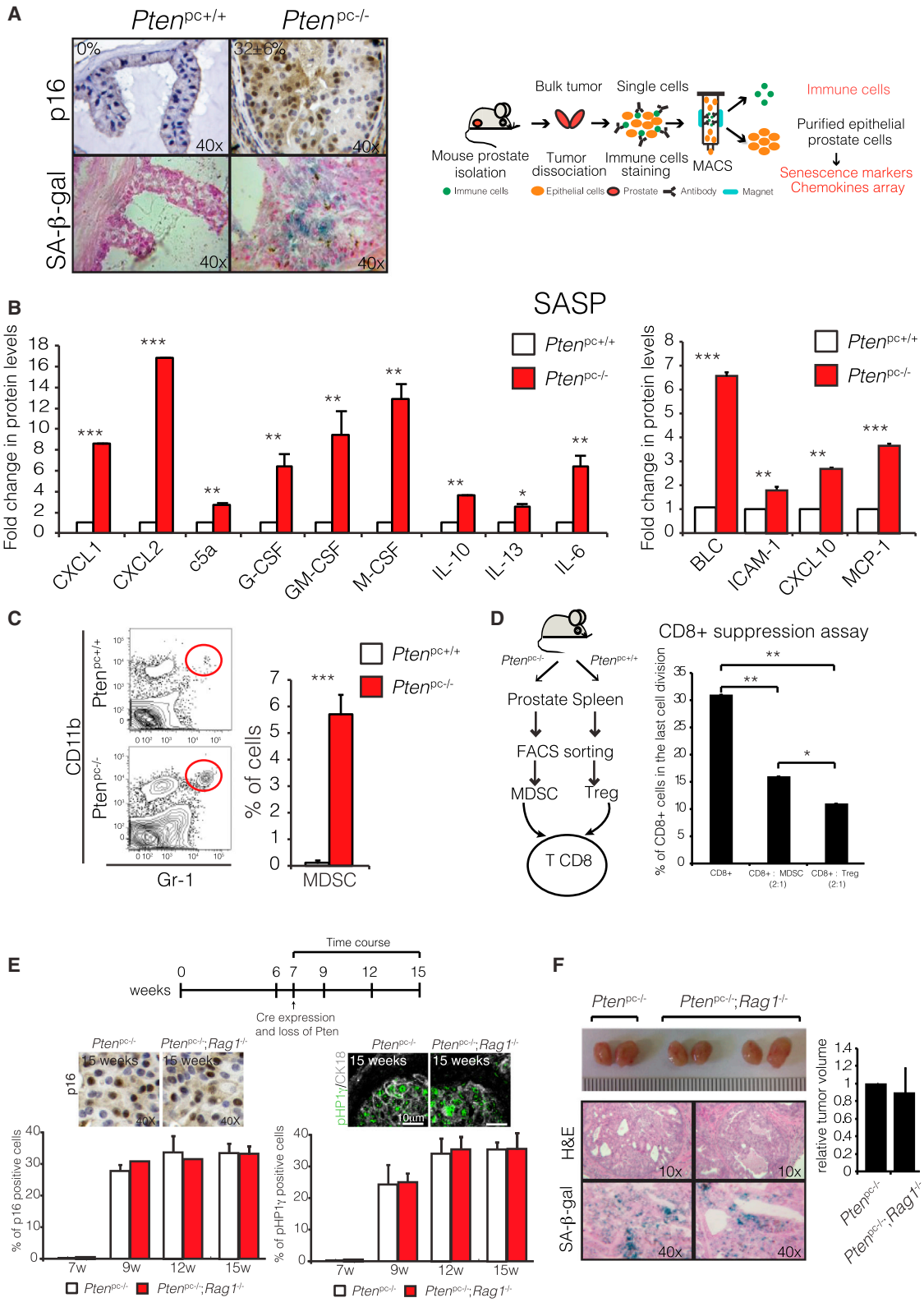

(legend on next page)

conditional mice (*Pten*$^{pc-/-}$) develop a prostatic intraepithelial neoplasia (PIN) characterized by a strong senescence response that progresses to invasive adenocarcinoma. This suggests that the SASP of *Pten*$^{pc-/-}$ tumors may drive protumorigenic rather than antitumorigenic effects. Thus, the concomitant presence of a senescent component and a proliferative compartment within the same tumor, along with a previously uncharacterized SASP and tumor immune response, makes *Pten*$^{pc-/-}$ mice a suitable mouse model to study the composition of the SASP and develop treatments that reprogram the protumorigenic effects of the senescence secretome.

RESULTS

Pten-Null Senescent Tumors Are Characterized by an Immunosuppressive Tumor Microenvironment

Starting from 7 weeks of age, *Pten*$^{pc-/-}$ mice develop PIN, a premalignant prostatic lesion characterized by a strong senescence response, as indicated by the senescence-associated β-galactosidase (SA-β-gal) positivity; fluorescein di-β-D-galactopyranoside staining; and increased expression of p16, p21, and plasminogen activator inhibitor-1 (Figures 1A, left, and S1A; Collado and Serrano, 2006). To characterize the cytokine profile of *Pten*$^{pc-/-}$ senescent tumors, we used magnetic-activated cell sorting (MACS) to isolate and separate prostate epithelial cells from both stromal and immune cells (Figure 1A, right). The efficiency of purification was controlled by fluorescence-activated cell sorting (FACS) analysis (Figure S1B). Purified *Pten*$^{pc-/-}$ epithelial cells were lysed and protein extracts loaded in a cytokine protein array to allow high-throughput multianalyte profiling of 40 different cytokines. Interestingly, the SASP of PICS was characterized by increased levels of several cytokines reported to play a negative role in cancer by favoring an immune-suppressive tumor microenvironment (Vanneman and Dranoff, 2012; Acharyya et al., 2012; Ostrand-Rosenberg and Sinha, 2009; Figures 1B, left, and S1C). However, potent chemoattractant cytokines that have been previously shown to play a role in the process of inflammation associated to senescence surveillance in OIS (Xue et al., 2007) were also upregulated in *Pten*$^{pc-/-}$ senescent tumors (Figures 1B, right, and S1C). In line with the cytokine array profile, FACS analysis showed that *Pten*$^{pc-/-}$ tumors were strongly infiltrated by CD11b^{+}Gr-1^{+} myeloid cells, in absence of CD4^{+}, CD8^{+}, and natural killer (NK) infiltrates (Figures 1C and S1D). CD11b^{+}Gr-1^{+} myeloid cells were granulocytic myeloid-derived suppressor cells (MDSCs) (Figure S1E), an immune-suppressive subset that blocks both proliferation and activity of CD4+, CD8+, and NK cells (Gabrilovich and Nagaraj, 2009). To assess the suppressive activity of CD11b^{+}Gr1^{+} cells in vivo, we sorted these cells directly from the *Pten*$^{pc-/-}$ tumors and cocultured them with CD8^{+} T cells. Notably, tumor-infiltrating CD11b^{+}Gr1^{+} cells suppressed the proliferation of CD8^{+} T cells (Figure 1D). Presence of MDSCs explained why CD8^{+} T and NK cells recovered from *Pten*$^{pc-/-}$ tumors were not cytotoxic (Figure S1F and S1G).

Recent evidence in a different mouse model indicates that senescent tumor cells are cleared by the immune system, a process termed senescence surveillance. Impairment of this response results in the development of aggressive tumors because the remaining senescent cells support tumorigenesis by secreting a variety of cytokines that favor the growth of non-senescent tumor cells (Xue et al., 2007; Kang et al., 2011). We then speculated that the immunosuppressive tumor microenvironment of *Pten*$^{pc-/-}$ tumors could impair senescence surveillance sustaining tumor progression. We therefore monitored the number of senescent cells in *Pten*$^{pc-/-}$ tumors at different times (from 7 to 15 weeks of age; Trotman et al., 2003). Interestingly, the percentage of senescent cells in *Pten*$^{pc-/-}$ tumors remained constant over time (Figure 1E), in contrast with previous findings in OIS (Kang et al., 2011). These data suggest that, in *Pten*$^{pc-/-}$ tumors, the adaptive immunity could be impaired, explaining why senescent tumor cells were not removed. To validate this hypothesis, we generated the *Pten*$^{pc-/-}$; *Rag1*$^{-/-}$ mouse model to induce PICS in a genetic background that lacks adaptive immunity (Figure S1H; Mombaerts et al., 1992). Consistent with our hypothesis, *Pten*$^{pc-/-}$; *Rag1*$^{-/-}$ mice developed prostate tumors with size and histology comparable to *Pten*$^{pc-/-}$ mice (Figure 1F; Kang et al., 2011). More importantly, the percentage of p16 and pHP1γ-positive cells and SA-β-gal staining between *Pten*$^{pc-/-}$ and *Pten*$^{pc-/-}$; *Rag1*$^{-/-}$ tumors remained comparable over time (Figures 1E and 1F). Altogether, these data indicate that senescent cells are not removed by the adaptive immunity in *Pten*$^{pc-/-}$ tumors, in contrast with previous findings in OIS (Kang et al., 2011). Therefore, the lasting senescent cells in these tumors may become a source of mitogenic cytokines that promote tumor progression.

The Jak2/Stat3 Pathway Is Activated in *Pten*$^{pc-/-}$ Senescent Tumors

The SASP of PICS pointed to Stat3 as a putative orchestrator of this immunosuppressive cytokine network (Yu et al., 2009). Indeed, several cytokines secreted by *Pten*$^{pc-/-}$ tumors such as (C-X-C motif) ligand 1 (CXCL1), CXCL2, interleukin-6 (IL-6), and IL-10 are transcriptionally regulated by Stat3. Therefore, we checked the status of Stat3 phosphorylation in *Pten*$^{pc-/-}$

Figure 1. Immunosuppressive Microenvironment in PICS

(A) p16 IHC and β-galactosidase staining in *Pten*$^{pc+/+}$ and *Pten*$^{pc-/-}$ mice (left). Experimental setup (right).

(B) Cytokine protein profile of purified prostatic epithelial cells isolated from prostates of 8-week-old *Pten*$^{pc+/+}$ and *Pten*$^{pc-/-}$ mice (n = 3; *p < 0.05; **p < 0.01; ***p < 0.001).

(C) FACS analysis of tumor-infiltrating CD11b^{+}Gr1^{+} immune cells in *Pten*$^{pc-/-}$ tumors (n = 7; ***p < 0.001).

(D) Scheme (left) and quantification (right) of the CD8^{+} suppression assay (see also Experimental Procedures). Immune-suppressive spleenic Treg was used as a positive control. (n = 3 to 4; *p < 0.05; **p < 0.01).

(E) Quantification of p16 and pHP1γ-positive cells in *Pten*$^{pc-/-}$ and *Pten*$^{pc-/-}$; *Rag1*$^{-/-}$ tumors at different time points. Insets are representative images from p16 IHC and pHP1γ IF staining (CK18 = cytokeratin 18 in gray).

(F) Gross anatomy (top), hematoxylin and eosin (H&E), β-galactosidase staining (bottom), and relative tumor volume (right) of anterior prostates (APs) in *Pten*$^{pc-/-}$ and *Pten*$^{pc-/-}$; *Rag1*$^{-/-}$ mice at 15 weeks of age (n = 4). Data are represented as mean ± SEM.

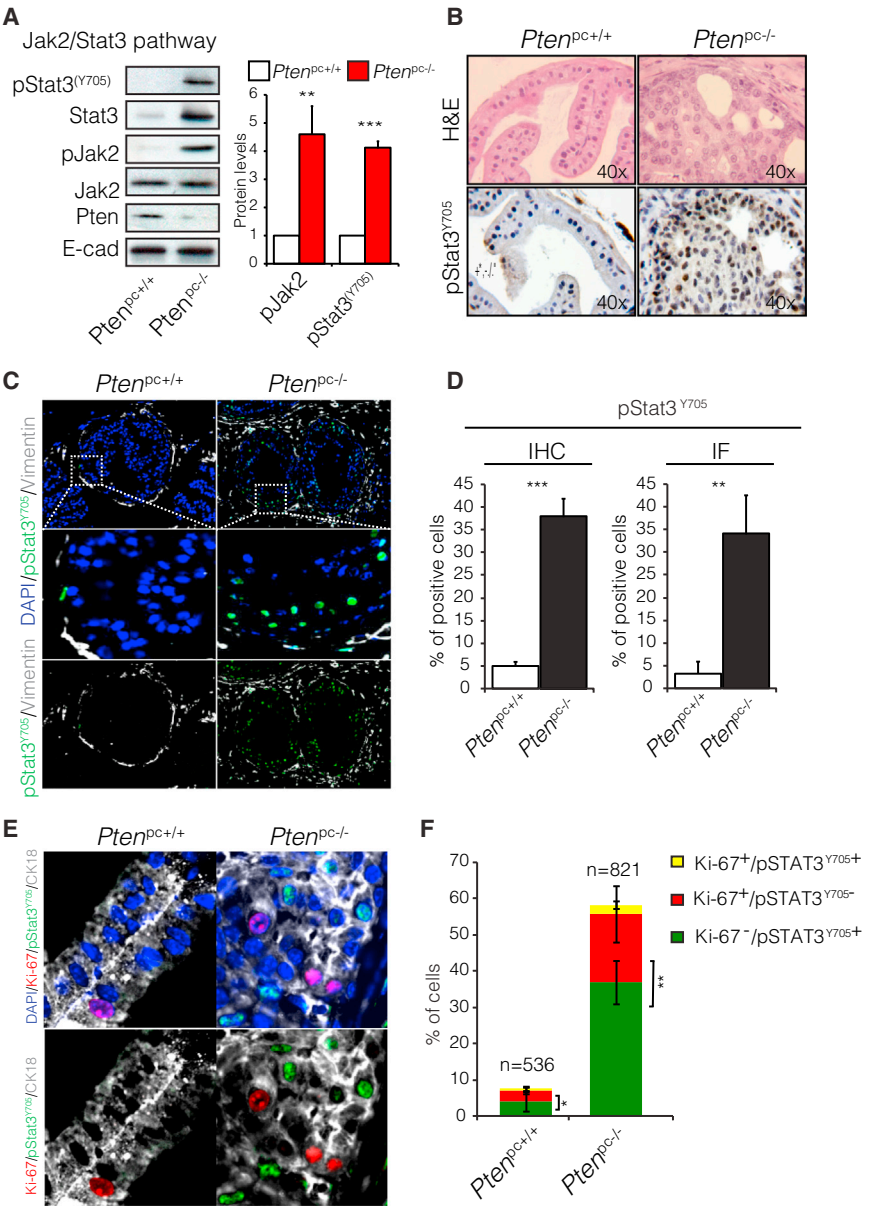

Figure 2. Stat3 Is Activated in Nonproliferating Cells in *Pten*$^{pc-/-}$ Tumors

(A) Western blot analysis and quantification (n = 4) showing activation of the Jak2/Stat3 pathway in *Pten*$^{pc-/-}$ tumors.

(B) H&E and pStat3$^{(Y705)}$ staining in AP lobes of *Pten*$^{pc+/+}$ and *Pten*$^{pc-/-}$ at 12 weeks of age.

(C) Confocal immunofluorescence (IF) images on *Pten*$^{pc+/+}$ and *Pten*$^{pc-/-}$ paraffin-embedded APs tumor sections (n = 3) in blue nuclear marker (DAPI) and in green pStat3$^{(Y705)}$-positive cells.

(D) Quantification of (B) and (C); bars represent the percentage of pStat3$^{(Y705)}$-positive cells.

(E) Confocal IF images on *Pten*$^{pc+/+}$ and *Pten*$^{pc-/-}$ paraffin-embedded APs tumor sections. Nuclear marker DAPI (blue), proliferation marker Ki67 (red), pStat3$^{(Y705)}$ (green), and prostate marker CK18 (gray; n = 3).

(F) Quantification of (E), bars represent the percentage of pStat3$^{(Y705)}$ single-positive, Ki-67 single-positive, and pStat3$^{(Y705)}$ /Ki-67 double-positive cells (n = total number of cells counted on three different tumors). Data are represented as mean ± SEM (**p < 0.01; ***p < 0.001).

tumors. Western blot analysis, immunohistochemistry (IHC) staining, and immunofluorescence (IF) confocal imaging revealed that Stat3 was strongly phosphorylated on tyrosine 705 (Y705) in *Pten*$^{pc-/-}$ tumors when compared with normal prostates (Figures 2A–2D, S2A, and S2B). Note that *Pten*$^{pc+/-}$ mice, which develop nonsenescent PIN lesions at 5 months of age (Alimonti et al., 2010; Trotman et al., 2003), stained completely negative for pStat3 (Figures S2A and S2B). Phosphorylation of Stat3 in *Pten*$^{pc-/-}$ tumors was also associated with the increased phosphorylation (five times more than in normal prostate) of the nonreceptor Janus kinase 2 (Jak2) (Figure 2A), an upstream activator of Stat3 (Parganas et al., 1998). Interestingly, IF analysis on consecutive sections from *Pten*$^{pc-/-}$ tumors revealed that, at the onset of senescence (8–10 weeks), the majority of the pStat3-positive epithelial cells stained negative for the proliferation marker Ki-67 and positive for the senescence marker pHP1γ (Figures 2E, 2F, S2C, and S2D). Altogether, our data suggest that, at least in *Pten*$^{pc-/-}$ tumors, Stat3 is mainly activated in nonproliferating senescent cells, in agreement with recent evidence in a different mouse model (Jackson et al., 2012).

In *Pten*$^{pc-/-}$; *Stat3*$^{pc-/-}$ Senescent Tumors, the Antitumor Immune Response Is Reactivated

To study the role of Stat3 in PICS and specifically its contribution to the SASP, we crossed *Pten*$^{loxP/loxP}$; *Pb-Cre4* mice with the *Stat3*$^{loxP/loxP}$ mice (Akira, 2000) to generate the *Pten*$^{loxP/loxP}$; *Stat3*$^{loxP/loxP}$ *Pb-Cre4* mouse model (hereafter referred to as *Pten*$^{pc-/-}$; *Stat3*$^{pc-/-}$). We first confirmed prostate-specific deletion of both *Pten* and *Stat3* in the mouse prostate epithelium (Figure S3A). Next, we looked for the presence of senescence in the *Pten*$^{pc-/-}$; *Stat3*$^{pc-/-}$ tumors and found upregulation of both p53 protein levels and SA-β-gal-staining positivity, indicating that Stat3 was not needed for the execution and maintenance of PICS (Figures 3A and 3B). Next, we checked the status of NF-kB, whose function controls both cell-autonomous and non-cell-autonomous aspects of senescence (Chien et al., 2011), and found that NF-kB was activated to a similar extent in both *Pten*$^{pc-/-}$ and *Pten*$^{pc-/-}$; *Stat3*$^{pc-/-}$ tumors (Figure 3A). Importantly, *Stat3* inactivation in both normal and *Pten*-null prostate epithelium did not affect cell proliferation and apoptosis (Figures S3B and S3C). However, the SASP of *Pten*$^{pc-/-}$; *Stat3*$^{pc-/-}$ tumors had reduced levels of the immune-suppressive

chemokines (CXCL2, granulocyte colony-stimulating factor, granulocyte macrophage colony-stimulating factor [GM-CSF], macrophage colony-stimulating factor [M-CSF], C5a, IL10, and IL13), whereas retained high levels of potent chemoattractants for B and T cells such as B lymphocyte chemoattractant, monocyte chemoattractant protein-1 (MCP-1), and CXCL10 when compared to the SASP of *Pten*$^{pc-/-}$ tumors (Figure 3C; Ansel et al., 2002; Deshmane et al., 2009; Dufour et al., 2002). Taken together, these data demonstrate that inactivation of Stat3 in *Pten*-null tumors reprograms the SASP of PICS (hereafter referred to as R-SASP) without affecting proliferation, apoptosis, and NF-kB signaling. In line with our findings, *Pten*$^{pc-/-}$; *Stat3*$^{pc-/-}$ mice developed senescent tumors strongly infiltrated by immune cells. FACS analysis on the immune cell fraction of *Pten*$^{pc-/-}$; *Stat3*$^{pc-/-}$ tumors showed a strong reduction in the percentage of MDSCs (Figure 3D) and increased infiltration of CD8$^+$, NK, and B cells (Figures 3E and 3F). Interestingly, the infiltration of immune cells in the *Pten*$^{pc-/-}$; *Stat3*$^{pc-/-}$ mouse prostatic epithelium occurred progressively after Pb-*Cre* activation, reaching a maximum at 15 weeks of age (see Figure S3D). Moreover, in *Pten*$^{pc-/-}$; *Stat3*$^{pc-/-}$ tumors, both CD8$^+$ and NK cells were cytotoxic, as indicated by the expression of the degranulation marker CD107a (Alter et al., 2004; Figures 3G and S3E), and B cells were present both as plasma cells (CD19$^+$B220$^-$) and antigen-presenting cells (CD19$^+$B220$^+$; Figure S3F). Restoration of the immune response in *Pten*$^{pc-/-}$; *Stat3*$^{pc-/-}$ tumors was also associated with a marked and progressive decrease in *p16* mRNA levels (Figure S3G) and a concomitant increase in *GranzymeB* mRNA levels at 15 weeks of age (Figure 3H). These data suggest that senescent cells were progressively cleared in these tumors, in agreement with previous data in a different model (Kang et al., 2011). Notably, whereas at early stage of tumorigenesis, *Pten*$^{pc-/-}$; *Stat3*$^{pc-/-}$ and *Pten*$^{pc-/-}$ tumors had comparable tumor size, at late stages, *Pten*$^{pc-/-}$; *Stat3*$^{pc-/-}$ tumors were smaller in size (roughly 70%; Figures 3I, 3J, and Figure S4A) and presented a reduced stromal compartment (Figure S4B). Importantly, whereas the totality (100%) of *Pten*$^{pc-/-}$ mice developed invasive prostate cancer at late stage of tumorigenesis (>15 weeks), only 25% of aged match *Pten*$^{pc-/-}$; *Stat3*$^{pc-/-}$ tumors developed invasive prostate tumors (Figures 3J and 3K). All together, our data show that *Stat3* inactivation in *Pten*-deficient tumors promotes an immune response switch (from immunosuppressive to active immunosurveillance) by decreasing the levels of specific cytokines in the tumor microenvironment, thus unmasking the immunostimulatory features of the SASP.

Docetaxel Treatment Enhances Senescence but Does Not Cause Significant Tumor Regression in *Pten*-Null Prostate Tumors

We next investigated whether the SASP of PICS could limit the efficacy of treatments that enhance senescence in *Pten*-null tumors. Docetaxel is the gold standard therapy for recurrent prostate cancer patients that no longer respond to hormonal approaches and is the only US-Food-and-Drug-Administration-approved first-line chemotherapy in these patients (Antonarakis and Armstrong, 2011). Previous evidence showed that docetaxel opposes tumor formation by promoting senescence (Schwarze et al., 2005). We next checked whether docetaxel treatment could be effective in *Pten*$^{pc-/-}$ mice by enhancing senescence. Despite the fact that docetaxel treatment enhanced senescence in *Pten*-null tumors as measured by upregulation of both *p16*, *p21* mRNA levels and immunohistochemistry staining for p16 (Figures S5A and S5B), it did not trigger a significant reduction in tumor volume (Figure S5C, bottom). Moreover, we did not detect significant effect of docetaxel treatment on tumor histology (Figure S5C, top). Of note, the increase in p16 staining correlated with strong activation of pStat3 in tumors (Figure S5B, bottom) and absence of an antitumor immune response as shown by the low levels of *GranzymeB* mRNA levels (Figure S5D). Moreover, in *Pten*$^{pc-/-}$ tumors treated with docetaxel, both CD8$^+$ and the NK cells were not cytotoxic, as indicated by lack of the degranulation marker CD107a in those cells (data not shown). In summary, docetaxel treatment increased senescence but had modest activity in *Pten*$^{pc-/-}$ tumors. These data are highly relevant considering the frequent loss of PTEN in prostate cancer (Trotman et al., 2003). These findings are also in line with a recent study demonstrating lack of response to docetaxel in patients with prostate cancers with decreased levels of PTEN (Antonarakis et al., 2012).

Pharmacological Inhibition of the Jak2/Stat3 Pathway Leads to an Effective Antitumor Immune Response in Prostate Tumors Treated with Docetaxel

We next hypothesized that the modest efficacy of docetaxel in *Pten*-null tumors was related to the absence of an effective antitumor immune response. Driven by the genetic evidences obtained from *Pten*$^{pc-/-}$; *Stat3*$^{pc-/-}$ mice, we reasoned that pharmacological inhibition of the Jak2/Stat3 pathway could be an effective strategy to reprogram the SASP and restore an antitumor immune response in docetaxel-treated, *Pten*-deficient tumors. We tested this hypothesis in a preclinical trial by combining the JAK2 inhibitor NVP-BSK805 (Baffert et al., 2010; Marotta et al., 2011) with docetaxel in a cohort of *Pten*$^{pc-/-}$ mice (Figure 4A). In this respect, whereas docetaxel and NVP-BSK805 alone displayed a modest single-agent antitumor response, the combination of docetaxel and NVP-NSK805 led to a profound reduction in tumor size with near complete pathological responses and no evidence of tumor invasion (Figures 4B and 4C). As observed in *Pten*$^{pc-/-}$; *Stat3*$^{pc-/-}$ tumors, inhibition of the Jak2/Stat3 pathway reprogrammed the SASP in docetaxel-treated mice (Figure 4D), favoring an active immune response, as indicated by the strong infiltration of CD3$^+$ T cells and increased mRNA levels of the cytotoxic marker *GranzymeB* (Figures 4E and 4F). Of note, the increased intratumor levels of *GranzymeB* in mice treated with docetaxel+NVP-BSK805 were associated with an increased percentage of apoptotic cells, in agreement with the proapoptotic function of *GranzymeB* (Trapani and Sutton, 2003; Figure 4G). At 12 weeks of age, both docetaxel- and docetaxel+NVP-BSK805-treated tumors exhibited a strong senescence response, as indicated by SA-β-gal positivity (Figure 4H). However, only in mice treated with docetaxel+NVP-BSK805, senescent cells were surrounded by T cells (Figure 4H). As a consequence, the percentage of senescent cells was strongly reduced in mice treated with NVP-BSK805 alone or in combination with docetaxel (Figure 4I). These data demonstrate that treatments targeting the Jak/Stat3 pathway may be

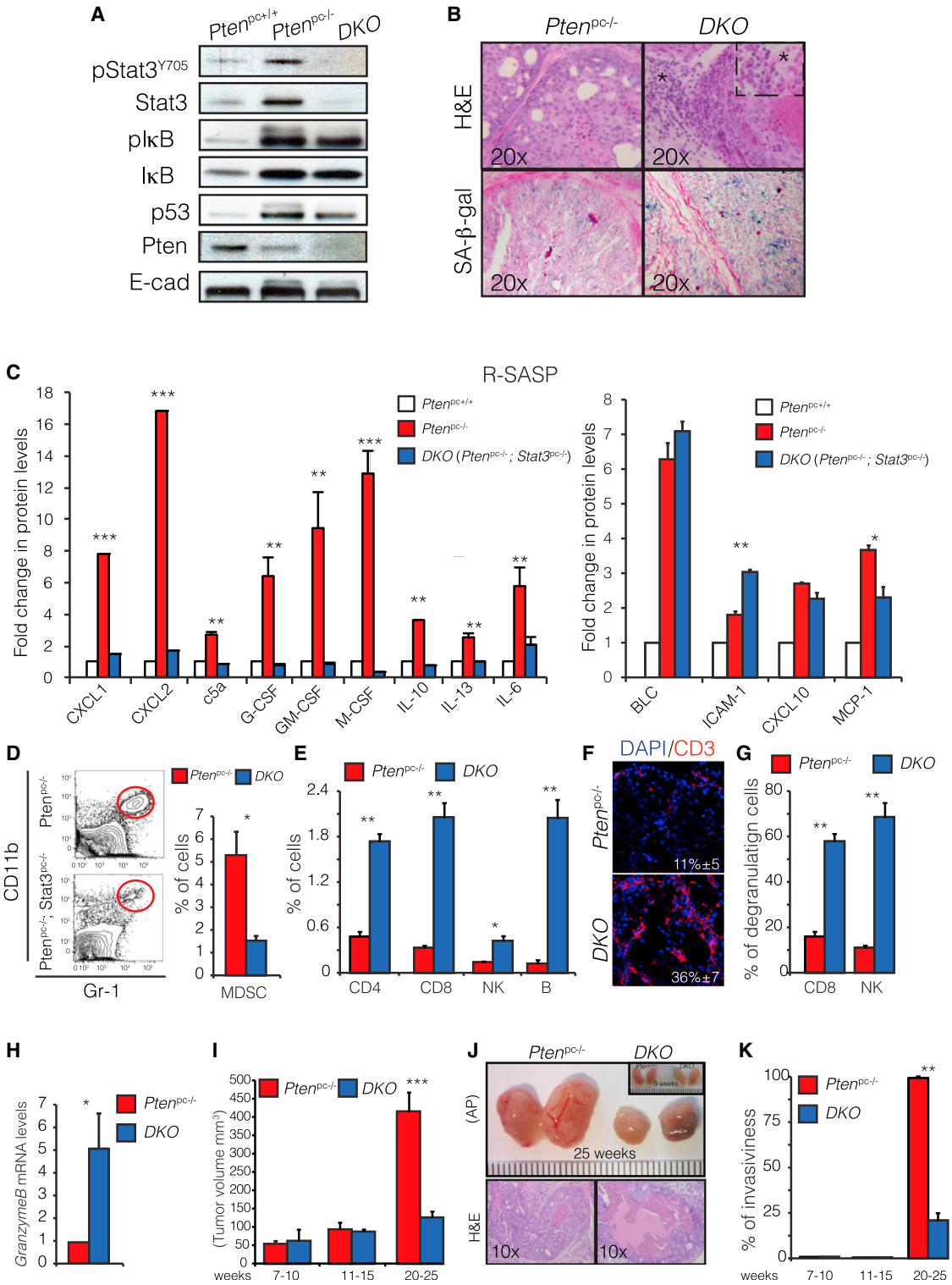

Figure 3. SASP Reprogramming Promotes an Antitumor Immune Response in *Pten*$^{pc-/-}$; *Stat3*$^{-/-}$ Mice

(A) Western blot showing the status of p53 and pIKBα in *Pten*$^{pc+/+}$, *Pten*$^{pc-/-}$, and *Pten*$^{pc-/-}$; *Stat3*$^{-/-}$ prostate tumors. DKO, double knockout.

(B) Representative images of SA-β-gal (bottom) and H&E (top) staining of *Pten*$^{pc-/-}$ and *Pten*$^{pc-/-}$; *Stat3*$^{-/-}$ tumors at 15 weeks. Images are magnified × 20. Inset shows infiltrated immune cells.

(C) Quantification of the cytokine protein profile of purified prostatic epithelial cell isolated from *Pten*$^{pc+/+}$, *Pten*$^{pc-/-}$, and *Pten*$^{pc-/-}$; *Stat3*$^{-/-}$ prostates (n = 3).

(legend continued on next page)

successfully used alone, or in combination with prosenescence compounds, to reprogram the SASP and promote an antitumor immune response in *Pten*-deficient tumors.

The Difference between the SASP of PICS and OIS Depends on the Genetic Background of the Senescent Tumor Cells

Previous findings demonstrate that the SASP of $Nras^{G12V}$-driven senescent tumors trigger senescence surveillance and tumor clearance (Kang et al., 2011). However, the SASP of PICS lacks this capability. We reasoned that the difference in the genetic background of senescent tumor cells could explain this phenomenon. To validate this hypothesis, we used the $Kras^{LSL\text{-}G12D/+}$; PbCre prostate conditional mouse model (hereafter referred as to Pb$Kras^{(G12D)}$) to compare the effects of the SASP of PICS and OIS in vivo (Tuveson et al., 2004). In agreement with previous findings, Pb$Kras^{(G12D)}$ mice developed hyperplasia/low-grade PIN in absence of invasive prostate cancer, even at late stage of disease (Figure 5A; Pearson et al., 2009). Notably, Pb$Kras^{(G12D)}$ prostate lesions from 14-week-old mice were senescent, as demonstrated by increased β-galactosidase staining and *p16* mRNA levels (Figures 5A and 5B). Next, we compared the SASP of PICS and OIS by analyzing prostate epithelial cells at the onset of senescence. Surprisingly, the immunosuppressive cytokines upregulated in PICS were only slightly increased in the secretome of OIS. Indeed, Pb$Kras^{(G12D)}$ tumors were characterized by lower levels of CXCL-2 and IL10 (Figure 5C). Moreover, in stark contrast to PICS, immunohistochemical analysis in Pb$Kras^{(G12D)}$ senescent tumors showed low level of Stat3 phosphorylation (Figure 5D). Immunophenotyping of Pb$Kras^{(G12D)}$ tumors revealed that $CD11b^{+}Gr1^{+}$ cells were almost undetectable when compared with the $Pten^{pc-/-}$ tumors (Figure 5E). Moreover, we found an increased percentage of interferon-γ releasing $CD8^{+}$-positive cells in Pb$Kras^{(G12D)}$ tumors (Figure 5F). Immune-mediated cytotoxic activity, measured by *GranyzmeB* mRNA levels, was also increased in these prostate lesions (Figure 5G). Importantly, in Pb$Kras^{(G12D)}$ tumor, senescent cells were progressively removed from the tumor, as indicated by the decay of SA-β-gal staining over time (Figure 5H), in agreement with previous findings in a different model of OIS (Kang et al., 2011). In summary, these findings suggest that activation of the Jak2/Stat3 pathway is the key determinant for the different SASPs and senescence-associated immune responses between PICS and OIS. Our data also suggest that compounds that target the JAK2/STAT3 pathway could be more effectively used in PTEN-null tumors rather than in tumors driven by activation of the mitogen-activated protein kinase pathway.

Loss of *PTEN* Drives Downregulation of *PTPN11/SHP2* that Sustains the Activation of the JAK2/STAT3 Pathway

We next sought the mechanism that leads to increased activation of the Jak2/Stat3 pathway in *Pten*-null senescent tumors by focusing on intrinsic regulatory negative systems of this pathway. Protein tyrosine phosphatase (PTP) SHP2 (also known as PTPN11) is one of the major negative regulators of the JAK2/STAT3 pathway. Indeed, hepatocyte-specific deletion of Shp2 in mouse promotes inflammation and tumorigenesis through the activation of Stat3 (Bard-Chapeau et al., 2011). Interestingly, *Shp2* mRNA levels were strongly reduced in $Pten^{pc-/-}$ tumors when compared to Pb$Kras^{(G12D)}$ tumors and normal prostates (Figure 6A). Western blot analysis confirmed that the levels of Shp2 were reduced in $Pten^{pc-/-}$ tumors at the onset of senescence (Figure 6B). To functionally validate these results in human cancer cell lines, we generated a doxycycline-inducible *sh-PTEN* DU-145 prostate stable cell line (DU-$145^{sh\text{-}PTEN}$) (Figure S6A). DU-145 cells retain 50% of the endogenous level of PTEN. Strikingly, further downregulation of *PTEN* was accompanied by the concomitant reduction in both SHP2 protein and mRNA levels and increased phosphorylation of STAT3 at steady state (Figures 6C and S6A). Similar results were also obtained in DU-145 cells when *PTEN* was downregulated by mean of two different small interfering RNAs (siRNAs) (Figure S6B). Moreover, in a time course experiment, we found that, when DU-$145^{sh\text{-}PTEN}$ cells were starved and stimulated with recombinant IL-6, phosphorylation of STAT3 lasted longer in cells induced with doxycycline (Figure 6D). Finally, rescue experiments showed that, when wild-type (WT) SHP2 was overexpressed in DU-145 cells in presence of si*PTEN*, the levels of pSTAT3 were reduced (Figure S6C). Consistently, *PTPN11/SHP2* downregulation by mean of siRNA in both DU-145 cancer cells and RWPE-1 untransformed cells led to an increase of pSTAT3 protein levels (Figure S6D). These data demonstrate that downregulation of PTEN and SHP2 directly sustained JAK2/STAT3 activation. Note that *Shp2* mRNA level remained downregulated in $Pten^{pc-/-}$; $Stat3^{pc-/-}$ tumors as well, suggesting that Shp2 is not under the transcriptional control of Stat3 (Figure S6E). Broad bioinformatics analysis conducted on ten different data sets of human prostate cancer (n = 1,086) confirmed the correlation between *PTEN* and *SHP2* (Figures 6E and S6F). Moreover, patients with low levels of both *PTEN* and *SHP2* had a worse prognosis when compared with the other groups (Figure 6F). Lastly, the correlation between PTEN and SHP2 was also validated in a human prostate cancer

(D) FACS analysis of tumor-infiltrating $CD11b^{+}Gr\text{-}1^{+}$ immune cells in $Pten^{pc-/-}$ and $Pten^{pc-/-}$; $Stat3^{-/-}$ (n = 4; *p < 0.05) tumors.
(E) Immunophenotyping of $Pten^{pc-/-}$; $Stat3^{-/-}$ tumors (n = 3; *p < 0.05; **p < 0.01).
(F) IF showing tumor-infiltrating $CD3^{+}$ cells in $Pten^{pc-/-}$ and $Pten^{pc-/-}$; $Stat3^{-/-}$ prostate tumors.
(G) Quantification by FACS analysis of $CD8^{+}$ and $NK1.1^{+}$ degranulation (n = 3; **p < 0.01).
(H) *GranzymeB* mRNA levels in $Pten^{pc-/-}$; $Stat3^{-/-}$ tumors (n = 3; *p < 0.05).
(I) Relative tumor volume of $Pten^{pc-/-}$ and $Pten^{pc-/-}$; $Stat3^{-/-}$ APs at different weeks (each group n = 3–6; ***p < 0.001).
(J) Gross anatomy and H&E staining of representative $Pten^{pc-/-}$ and $Pten^{pc-/-}$; $Stat3^{-/-}$ APs from 20- to 25-week-old mice. Images are magnified × 10. Inset shows APs from $Pten^{pc-/-}$ and $Pten^{pc-/-}$; $Stat3^{-/-}$ at 9 weeks.
(K) Percentage of mice presenting an invasive phenotype in APs from $Pten^{pc-/-}$ and $Pten^{pc-/-}$; $Stat3^{-/-}$ tumors at different weeks (each group n = 3; ***p < 0.001).
Data are represented as mean ± SEM.

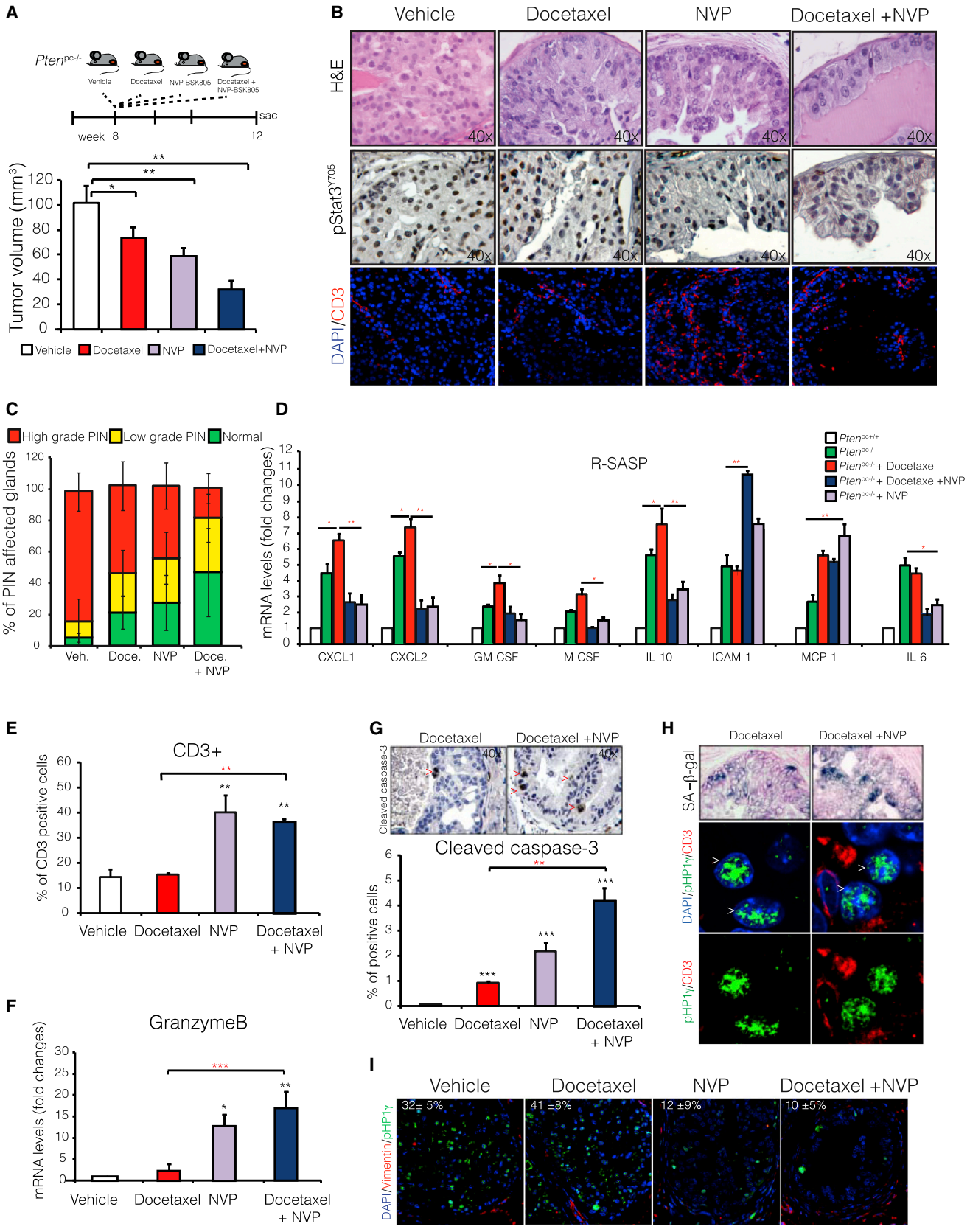

(legend on next page)

tissue microarray (TMA) (Figure 6G). In agreement with our data in mouse models, we also found a strong anticorrelation between decreased PTEN and SHP2 levels ($PTEN^{low}SHP2^{low}$) and increased JAK2 phosphorylation in human prostate tumors (Figure 6G). Of note, this anticorrelation appeared even stronger in prostate cancers with high Gleason score ($\geq$7; Figure 6H). These findings support the emerging view of *SHP2* as potential tumor suppressor also in prostate cancer in line with recent evidence in other tumor types (Bard-Chapeau et al., 2011; Chan and Feng, 2007; Yang et al., 2013). Finally, *PTEN* and *SHP2* correlation was also found in a PANCANCER analysis including 5,703 tumor samples of different histology such as breast, melanoma, lung adenocarcinoma, kidney, and clear cell carcinoma (Figures 7A, S7A, and S7B). As found for prostate cancer patients, low levels of both *PTEN* and *SHP2* were also associated with the worst clinical outcome (Figure 7B).

This finding suggests that the correlation between *PTEN* and *SHP2* levels is a general phenomenon frequently observed in a variety of tumors at different stages of disease.

DISCUSSION

The mechanisms that link the SASP to tumorigenesis are poorly understood and remain a subject of intense investigation and debate. On this line, different studies have reported that the SASP can exert pro- as well as antitumorigenic effects (Coppé et al., 2010; Kang et al., 2011; Xue et al., 2007; Rodier and Campisi, 2011; Davalos et al., 2010). However, there has been little investigation into the possibility to reprogram the SASP of a senescent tumor in order to abolish its protumorigenic effects while retaining its immunostimulatory features. In this study, we provide evidence that the SASP of senescent tumors can be both genetically and pharmacologically reprogrammed and that the efficacy of chemotherapy is enhanced in the context of R-SASP. Moreover, our findings demonstrate that the SASP of PICS is orchestrated by both NF-kB and Stat3 activation. Both genetic and pharmacological inactivation of the Jak2/Stat3 pathway does not abolish the SASP of PICS but drives an overall reprogramming of the senescence secretome retaining a positive NF-kB signature (Chien et al., 2011). On this line, the R-SASP of *Pten*-null senescent tumors has reduced levels of cytokines, such as CXCL1/CXCL2, GM-CSF, M-CSF, IL10, and IL13, involved in the recruitment and activation of MDSCs but retains increased levels of immunostimulatory chemokine such as MCP-1, previously shown to activate senescence surveillance (Gabrilovich and Nagaraj, 2009; Xue et al., 2007; Zitvogel et al., 2008). Importantly, we provide evidence that R-SASP improves chemotherapy efficacy in *Pten*-null tumors. Indeed, docetaxel drives a strong senescence response in *Pten*-null tumors but fails to activate an antitumor immune response and tumor clearance. These findings have immediate implications for the design of clinical trials evaluating the efficacy of docetaxel or novel chemotherapies, whose mechanism of action is based on senescence induction in prostate cancer patients. Our preclinical data predict that single-agent docetaxel will mostly result in disease stabilization, rather than tumor regression, particularly in PTEN-null tumors that account for the majority of primary and metastatic prostate cancers and that often retain an intact p53 status (Schlomm et al., 2008). A recent clinical trial demonstrates that PTEN-deficient prostate cancer patients are resistant to docetaxel treatment in line with our findings in the mouse model (Antonarakis et al., 2012). In this respect, our data suggest that combined therapy with JAK inhibitors should promote the reprogramming of the SASP, leading to an antitumor immune response in docetaxel-treated patients (Figure S7C, model).

In addition, the direct comparison between two different types of senescence responses in prostate, PICS versus OIS, provides insights on the mechanisms that lead to the establishment of a protumorigenic SASP in senescent tumors. Indeed, in Pb*Kras*$^{(G12D)}$-driven senescent tumors (OIS), and in stark contrast to PICS, we did not observe downregulation of SHP2 and activation of Stat3. Absence of Stat3 activation in OIS was associated with a distinct SASP compared to PICS, which was characterized by a lower level of immune-suppressive chemokines and high levels of chemoattractants. This explains the absence of tumor-infiltrating MDSCs, the strong activation of T cells, and the progressive decay in the number of senescence tumor cells in OIS. Because the effects of the SASP have been recently shown to be spatially restricted, it is possible that the levels of the immunosuppressive chemokines secreted by OIS are not sufficient to exert prominent paracrine effects on the tumor microenvironment (Acosta et al., 2013).

Lack of senescence surveillance in PICS, but not OIS, may explain at least in part why *Pten*-null prostate tumors became invasive at late stage whereas Pb*Kras*$^{(G12D)}$ mice develop only benign tumor lesions. All together, these data suggest that

Figure 4. SASP Reprogramming Enhances Docetaxel Efficacy in *Pten*$^{pc-/-}$ Tumors

(A) Schedule of treatment used in the preclinical trial with the Jak2 inhibitor NVP-BSK805 and docetaxel in *Pten*$^{pc-/-}$ mice. Starting from 8 weeks of age, mice were treated daily for 4 weeks with a dose of 100 mg/kg of NVP-BSK805 alone or in combination with weekly docetaxel at 10 mg/kg (top). Analysis of tumor volume in the indicated treatment groups (bottom; n = 6–10; *p < 0.05; **p < 0.01).

(B) H&E, pStat3^{y705}, and CD3 staining in *Pten*$^{pc-/-}$ tumors treated with NVP-BSK805, docetaxel, and docetaxel+NVP-BSK805. pStat3 staining is used as control to assess inhibition of the Jak2/Stat3 pathway after treatment with NVP-BSK805.

(C) Quantification of PIN-affected glands after the treatments.

(D) Cytokine profile of the reprogrammed SASP (R-SASP) in the indicated treatment groups (n = 5; *p < 0.05; **p < 0.01; mice = 12 weeks of age).

(E) Quantification of the tumor-infiltrating CD3$^+$-positive cells shown in (B) (n = 3; **p < 0.01).

(F) *GranzymeB* mRNA levels in *Pten*$^{pc-/-}$ tumors treated with NVP-BSK805-, docetaxel-, and docetaxel+NVP-BSK805-treated tumors (n = 3; *p < 0.05; **p < 0.01; ***p < 0.001).

(G) Quantification of cleaved-caspase 3-positive cells (n = 3; ***p < 0.001).

(H) IF confocal images showing the localization of CD3$^+$-positive cells (red) in close proximity of senescent cells (green).

(I) Representative IF confocal images showing the percentage of pHP1γ-positive senescent cells (green) in *Pten*$^{pc-/-}$-treated mice. Data are represented as mean ± SEM.

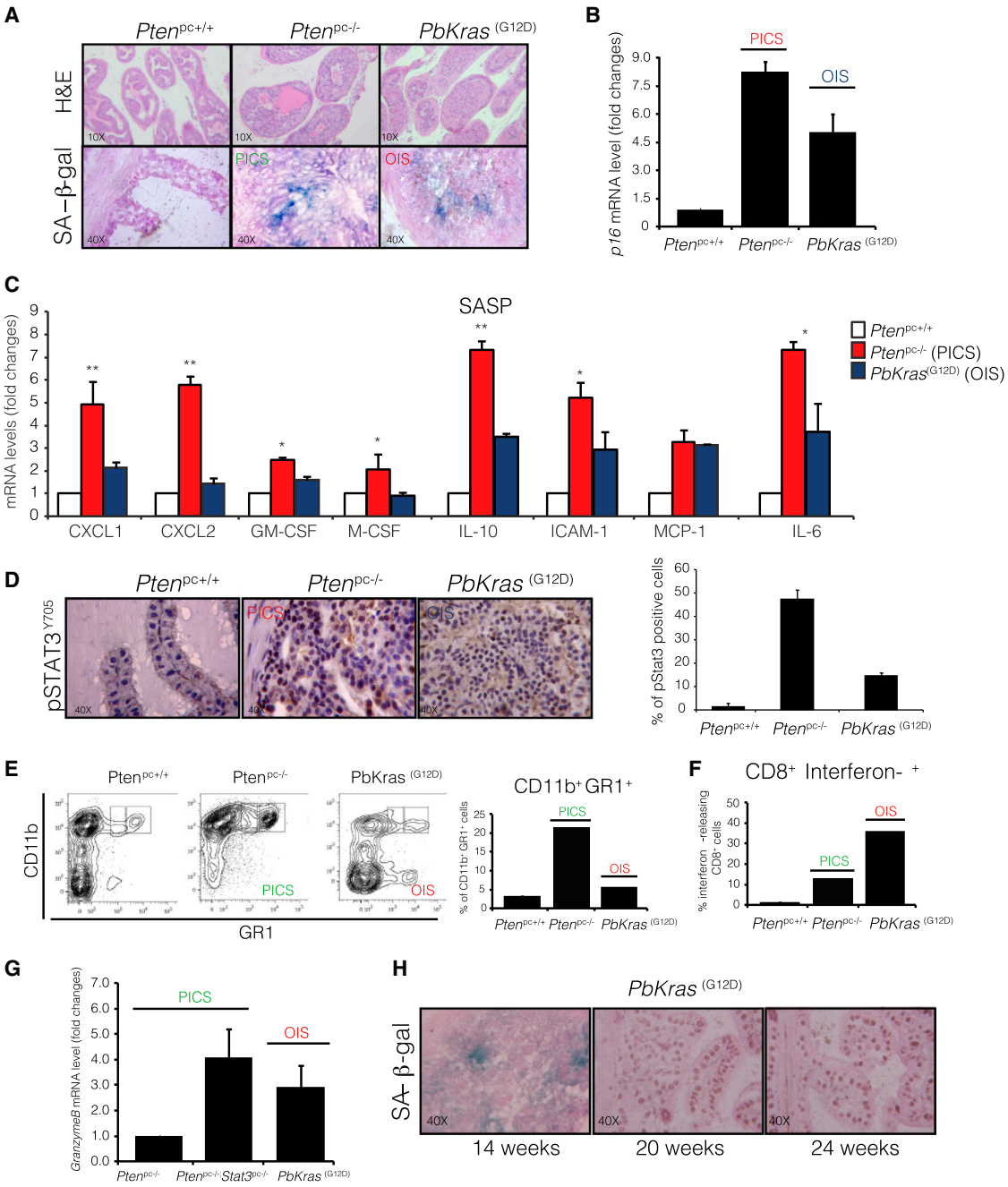

Figure 5. Comparative Analysis of PICS versus OIS in Prostates

(A) H&E (top) and β-galactosidase staining (bottom) of *Pten*$^{pc+/+}$, *Pten*$^{-/-}$, and *Kras*$^{(G12D)}$ prostates at 14 weeks of age.

(B) p16 mRNA levels in *Pten*$^{pc+/+}$, *Pten*$^{pc-/-}$ (PICS), and *Kras*$^{(G12D)}$ (OIS) prostates.

(C) Different SASP intensity between PICS and OIS (n = 3; *p < 0.05; **p < 0.01).

(D) pStat3^{Y705} staining (left) and its quantification (right) on paraffin sections from *Pten*$^{pc+/+}$, *Pten*$^{pc-/-}$ (PICS), and *Kras*$^{(G12D)}$ (OIS) prostates (n = 3).

(E) FACS analysis (and quantification of CD11b^{+}GR1^{+} cells in *Pten*$^{pc+/+}$, *Pten*$^{pc-/-}$ [PICS], and *Kras*$^{(G12D)}$ [OIS] prostates). Percentages calculated on CD45^{+}-gated cells.

(F) Percentage of interferon-γ-releasing CD8^{+} cells (gated on CD45^{+} cells) in *Pten*$^{pc+/+}$, *Pten*$^{pc-/-}$ (PICS), and *Kras*$^{(G12D)}$ (OIS) prostates (n = 3).

(G) *GranzymeB* mRNA levels in *Pten*$^{pc-/-}$ (PICS), *Pten*$^{pc-/-}$; *Stat3*$^{pc-/-}$ (PICS), and *Kras*$^{(G12D)}$ (OIS) senescent prostate tumors (n = 3).

(H) Representative images showing the decay of SA-β-galactosidase staining over time (14, 20, and 24 weeks) in *Kras*$^{(G12D)}$ tumors.

Data are represented as mean ± SEM.

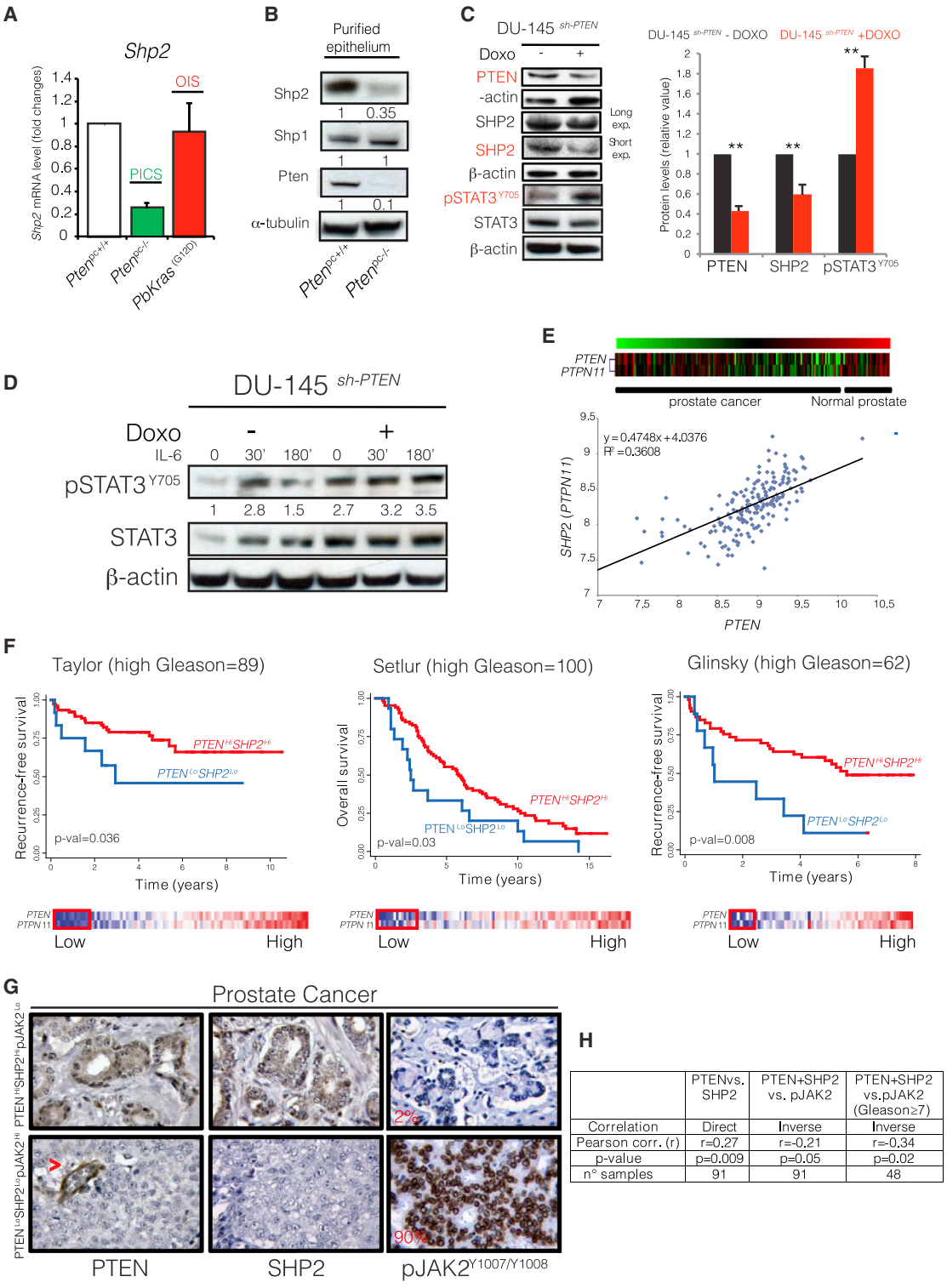

	PTENvs. SHP2	PTEN+SHP2 vs. pJAK2	PTEN+SHP2 vs.pJAK2 (Gleason≥7)
Correlation	Direct	Inverse	Inverse
Pearson corr. (r)	r=0.27	r=-0.21	r=-0.34
p-value	p=0.009	p=0.05	p=0.02
n° samples	91	91	48

Figure 6. Correlation between PTEN and PTPN11/SHP2 Levels in Both Mouse and Human Prostate Cancers

(A) *Shp2* mRNA levels in *Pten*$^{pc+/+}$, *Pten*$^{pc-/-}$ (PICS), and in *Kras*$^{(G12D)}$ (OIS) tumors (n = 3; **p < 0.01).

(B) Western blot analysis showing the reduced Shp2 protein levels in *Pten*$^{pc+/+}$ and *Pten*$^{pc-/-}$ purified epithelial prostate cells at the onset of senescence (8 weeks *Pten*$^{pc-/-}$ tumors; high-grade PIN and 14 weeks *Kras*$^{(G12D)}$; low-grade PIN).

(C) Western blot analysis and quantification of PTEN, SHP2, and STAT3 levels in DU-145 human prostate tumor cells infected with an inducible small hairpin RNA for PTEN.

(legend continued on next page)

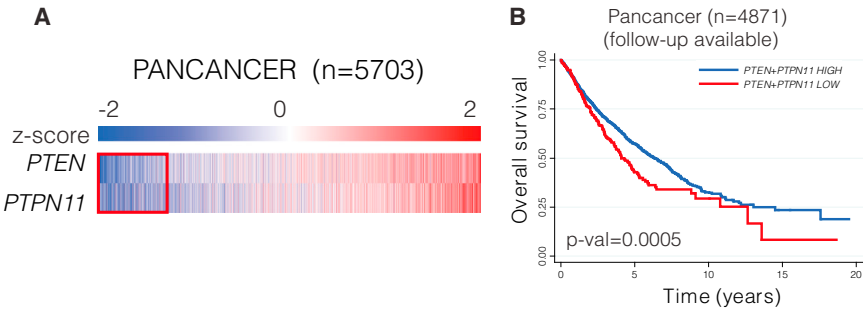

Figure 7. The Correlation between *PTEN* and *PTPN11/SHP2* Is Frequently Found in Cancer

(A) Heatmap showing the correlation between *PTEN* and *PTPN11/SHP2* in a PANCACER analysis performed on 25 different tumor types (5,703 samples).

(B) Overall survival showing the poor clinical outcome of patients with low levels of both *PTEN* and *PTPN11/SHP2* (red line) when compared with the group of patients with high levels of both *PTEN* and *PTPN11/SHP2* (blue line); the group of patients with low levels of both *PTEN* and *PTPN11/SHP2* are the patients highlighted in the red box of the heatmap of (A).

activation of Jak2/Stat3 pathway is the key determinant underlying the difference between the SASPs of PICS and OIS and demonstrate that the protumorigenic features of the SASP depend on the genetic background of senescent tumor cells.

Our findings establish a direct correlation between the levels of PTEN and SHP2 in both mouse and human tumors. Recent studies have demonstrated that loss of SHP2 activity or deletion of *Ptpn11*, the gene encoding for SHP2, promote tumorigenesis in different mouse models by sustaining the activation of the JAK/STAT3 pathway (Bard-Chapeau et al., 2011; Zhu et al., 2013; Yang et al., 2013). Our PANCANCER analysis also demonstrated that the correlation between the levels of *PTEN* and *SHP2* exist in different types of human tumors in addition to prostate cancer. Finally, patient stratification based on the levels of *PTEN* and *SHP2* showed that tumors with low levels of both *PTEN* and *SHP2* had the worst prognosis, reinforcing the potential clinical implication of our findings also in a broader scenario beyond the context of senescence tumor lesions.

EXPERIMENTAL PROCEDURES

Mice

$Pten^{loxP/loxP}$ mice were generated and genotyped as previously described (Alimonti et al., 2010; Chen et al., 2005; Trotman et al., 2003). $Stat3^{loxP/loxP}$ mice were generated and provided by Oriental BioService. $Rag1^{-/-}$ mice were a kind gift from Prof. Fabio Grassi. Female $Pten^{loxP/loxP}$; $Stat3^{loxP/loxP}$ and $Pten^{loxP/loxP}$; $Rag1^{-/-}$ mice were crossed with male *PB-Cre4* transgenic mice and genotyped. For *Stat3*, $Stat3^{loxP/loxP}$ primer 1 (5′-CCTGAAGACCAAGTTCAT CTGTGTGAC-3′) and primer 2 (5′-CACACAAGCCATCAAACTCTGGTCTCC-3′) were used. For $Rag1^{-/-}$ primer 1 (5′-GAGGTTCCGCTACGACTCTG −3′) and primer 2 (5′-CCGGACAAGTTTTTCATCGT-3′) primer 3 (Neo; 5′-TGGATGTG GAATGTGTGCGAG-3′) were used. All mice were maintained under specific pathogen-free conditions in the animal facilities of the Institute for Research in Biomedicine, and experiments were performed according to state guidelines and approved by the local ethics committee.

Western Blot, Immunohistochemistry, and Immunofluorescence

Tissue and purified epithelial lysates were prepared with RIPA buffer (1 × PBS, 1% Nonidet P40, 0.5% sodium deoxycholate, 0.1% SDS, and protease inhibitor cocktail [Roche]). The following antibodies were used for western blotting: rabbit polyclonal anti-Pten (9552; Cell Signaling Technology), rabbit monoclonal anti-phospho Stat3 Tyr705 (D3A7; CST), mouse monoclonal Stat3 (124H6; CST), rabbit monoclonal anti-Jak2 (D2E12; CST), rabbit polyclonal anti-phospho- Jak2 (3771; CST), rabbit polyclonal anti-Akt and anti-phosphoserine 473 of Akt (CST), rabbit polyclonal anti-p16 (M156; Santa Cruz Biotechnology), mouse monoclonal anti-β-actin (AC-74; Sigma), rabbit monoclonal anti-SHP-1 (C14H6; CST), and rabbit monoclonal anti-SHP-2 (D50F2; CST). For IHC, tissues were fixed in 10% formalin and embedded in paraffin in accordance with standard procedures. Sections were stained for phospho Stat3 Tyr705(D3A7; CST), Stat3 (124H6; CST), Pten (51-2400; Invitrogen), Ki67(Clone SP6; Lab Vision), anti-CD3 (Dako), and anti-CD45R/B220 (BD Pharmigen). For IF on tissue, paraffin-embedded sections were stained for rabbit monoclonal anti-phospho Stat3 Tyr705 (D3A7; CST) and mouse monoclonal anti-α-tubulin (DM1A; CST). Confocal sections were obtained with Leica TCS SP5 confocal microscope.

Prostatic Epithelial Cell Purification and Cytokine Array

$Pten^{pc+/+}$; $Stat3^{pc+/+}$; $Pten^{pc+/+}$, $Pten^{pc-/-}$, and $Pten^{pc-/-}$; $Stat3^{pc-/-}$ 9-week-old mice were scarified, and whole prostates (n = 3 per group) were isolated and processed to single-cell suspension (Lukacs et al., 2010) for MACS. Single cells were stained with fluorescein isothiocyanate (FITC)-anti-CD34 (stroma), FITC-anti-Ter119 (erythrocytes), FITC-anti-CD31 (endothelial), and FITC-anti-CD45 (leukocytes) and incubated 20 min on ice. All antibodies (BD Biosciences) were used at 1:300; cells were then loaded into MS column (Miltenyi Biotec) for MACS separation, and unstained epithelial cells were collected in the negative fraction. Purified prostatic epithelial cells were processed as indicated in cytokine array kit (R&D Systems). Developed films were scanned, obtained images were analyzed using ImageJ 1.43u, and background signals were subtracted from the experimental values.

Autopsy and Histopathology

Animals were autopsied, and all tissues were examined regardless of their pathological status. Normal and tumor tissue samples were fixed in 10% neutral-buffered formalin (Sigma) overnight. Tissues were processed by

(D) Time course experiment showing the sustained phosphorylation of STAT3 upon PTEN downregulation in DU-145 prostate cells. Cells were starved for 12 hr in presence of 0.5% of FCS and then stimulated with IL-6 (40 ng/ml) and STAT3 phosphorylation assessed by western blot at the indicated time points.

(E) Heatmaps and scattered plot showing the correlation between *PTEN* and *SHP2* mRNA levels in a human data set of normal prostates and prostate tumors (GSE21034).

(F) Kaplan-Meier survival curves of three different human prostate cancer data sets. The blue curve represents patients with low levels of both *PTEN* and *SHP2*; the red curve represents patients with high levels of both *PTEN* and *SHP2*.

(G) IHC for PTEN, SHP2/PTPN11, and pJAK2 on a tissue microarray (TMA) of human prostate cancer.

(H) Table showing the correlation between PTEN and SHP2/PTPN11 protein levels and the anticorrelation between the protein levels of PTEN-SHP2/PTPN11 and pJAK2; analysis performed on the TMA in (G). Data are represented as mean ± SEM. Images are magnified × 20.

ethanol dehydration and embedded in paraffin according to standard protocols. Sections (5 μm) were prepared for antibody detection and hematoxylin and eosin (H&E) staining. To evaluate evidence of invasion, sections were cut at 20 μm intervals and H&E stained. Slides were prepared containing three to five of these interval sections.

Flow Cytometry Analysis of Cell Phenotype

Samples were acquired on a BD FACSCanto II flow cytometer (BD Biosciences) after fixation with 1% formaldehyde (Sigma-Aldrich). Cells resuspended in PBS containing 1% fetal calf serum (FCS) (Sigma-Aldrich) were stained for 10 min at room temperature with the following anti-mouse monoclonal antibodies: CD45 eFluor 450 (clone 30-F11); CD3e FITC (clone 145-2C11); CD4 allophycocyanin (APC)-eFluor 780 (clone GK1.5); CD8 phycoerythrin (PE) (clone 53-6.7); CD25 PE-Cy7 (clone PC61.5); NK1.1 eFluor 450 (clone PK136); lysosomal-associated membrane protein 1 (CD107a) APC (clone 1D4B); Ly-6G (Gr-1) PE (clone RB6-8C5); CD11b APC (clone M1/70); CD19 FITC (clone 6D5); and CD45R/B220 FITC (clone RA3-6B2). All the antibodies were purchased from eBioscience. $GR1^+CD11b^+$ were sorted from the prostate single-cell suspension using a FACSAria cell sorter (BD Biosciences) after staining with anti-CD45, anti-GR1, and anti-CD11b antibodies for 30 min at 4°C in PBS containing 1% FCS. $CD8^+$ T cells were sorted based on the expression of CD45, CD3, and CD8. Data were analyzed using FlowJo software (TreeStar).

In Vitro Suppression Assay

In vitro suppression assays were carried out in RPMI/10% FCS in 96-well U-bottom plates (Corning) with 2.5×10^4 $CD8^+$ splenocytes as responder cells and titrated amounts of FACS-sorted $GR1^+CD11b^+$ or $CD3^+CD4^+CD25^+$ Treg used as a positive control. $CD8^+$ T cells were labeled with 5 μM CFSE (Molecular Probes), and stimulation was carried out with plate-bound anti-CD3 (3C11; 2 μg/ml) and anti-CD28 (2 μg/ml; BD PharMingen). After 4 days at 37°C, proliferation of $CD8^+$ T cells was analyzed by FACSCanto flow cytometer.

RNA Expression Analysis

RNA isolation (QIAGEN) and TaqMan reverse transcriptase reaction (Applied Biosystems) were according to the manufacturer's instructions. Quantitative PCR reactions (Bio-Rad) for each sample were done in triplicate. Sequences used for PAI-1, IL6, MCP-1, CXCL1, CXCL2, GM-CSF, M-CSF, IL10, ICAM-1, SHP2, PTEN, p21, p16, and GranzymeB were as follows: PAI-1 forward 5′-TTGAATCCCATAGCTGCTT-3′, reverse 5′-GACACGCCATAGGGAGAGA-3′; IL6 forward 5′-TAGTCCTTCCTACCCCAATTT-3′, reverse 5′-TTGGTCCTTAGCCACTCCTTC-3′; MCP-1 forward 5′-GTGGGGCGTTAAACTGCAT-3′, reverse 5′-CAGGTCCCTGTCATGCTTCT-3′; CXCL1 forward 5′-CTGGGATTCACCTCAAGAACATC-3′, reverse 5′-CAGGGTCAAGGCAAGCCTC-3′; CXCL2 forward 5′-CCAACCACCAGGCTACAGG-3′, reverse 5′-GCGTCACACTCAAGCTCTG-3′; GM-CSF forward 5′-GGCCTTGGAAGCATGTAGAGG-3′, reverse 5′-GGAGAACTCGTTAGAGACGACTT-3′; M-CSF forward 5′-TGCTAGGGGTGGCTTTAGG-3′, reverse 5′-CAACAGCTTTGCTAAGTGCTCTA-3′; IL-10 forward 5′-GCTCTTACTGACTGGCATGAG-3′, reverse 5′-CGCAGCTCTAGGAGCATGTG-3′; ICAM-1 forward 5′-GTGATGCTCAGGTATCCATCCA-3′, reverse 5′-CACAGTTCTCAAAGCACAGCG-3′; SHP2 forward 5′-GAACTGTGCAGATCCTACCTCT-3′, reverse 5′-TCTGGCTCTCTCGTACAAGAAA-3′; PTEN forward 5′-TGGATTCGACTTAGACTTGACCT-3′, reverse 5′-GGTGGGTTATGGTCTTCAAAAGG-3′; p21 forward 5′-CCCCCAATCGCAAGGATTCTT-3′, reverse 5′-CTTGGTTCGGTGGGTCTGTC-3′; p16 forward 5′-CGCAGGTTCTTGGTCACTGT-3′, reverse 5′-TGTTCACGAAAGCCAGAGCG-3′; and GranzymeB forward 5′-CCACTCTCGACCCTACATGG-3′, reverse 5′-GGCCCCCAAAGTGACATTTATT-3′.

Small Hairpin RNA, siRNA, and Plasmids

DU145 prostate cancer cell lines were plated into 6-well dishes and infected with a doxycycline-inducible pTRIPZ sh*PTEN* (clone id: V2THS_92317; Open Biosystems; mature sense: 5′ GGCGCTATGTGTATTATTA 3′). si*PTEN_1* (Life Technologies; cat. no. 4392420); si*PTEN_2* and *siPTPN11* (Thermo Scientific). Plasmid used for the rescue experiments: CMV566 empty vector and pCMV-SHP2 WT (Addgene).

Gene Expression Profiling

Prostate cancer genome-wide gene expression data sets and clinical information were downloaded from Gene Expression Omnibus database or obtained from authors upon request (Glinsky et al., 2004; Setlur et al., 2008; Taylor et al., 2010). Pancancer data set matrix and clinical information was downloaded from University of California, Santa Cruz Cancer Genomics Browser (https://genome-cancer.ucsc.edu). Human cancer cell lines expression data set and sensitivity values to docetaxel treatment (IC_{50} values) were downloaded from http://www.cancerrxgene.org/downloads (Garnett et al., 2012).

Correlation Analysis

Correlation between gene-expression-derived values in the principle-component analysis (PCA) and Pancancer data sets was done using Pearson correlation test, which estimates a correlation value "r" and a significance p value ($r > 0 < 1$, direct correlation; $r < 0 > -1$, inverse correlation). Correlation was also performed in TMA staining evaluation using the estimated percentage of positively stained cells as determined by a pathologist (M.S.).

Survival Curves

Differential survival between patient subgroups was plotted and calculated using Kaplan-Meier curves. Patients were stratified based on *PTEN* and *PTPN11* score values. In brief, scores were rank ordered and divided in seven percentiles (from lowest to highest values). We considered samples having *PTEN*/*PTPN11* low values as those in the first percentile. Such stratification gave significant differences in overall survival within the Pancancer study (log rank test) and in the high Gleason patients within the PCA data sets.

Statistical Analysis

Data analysis was performed using a two-tailed unpaired Student's t test. Values are expressed as mean ± SEM (*$p < 0.05$; **$p < 0.01$; ***$p < 0.001$).

SUPPLEMENTAL INFORMATION

Supplemental Information includes seven figures and can be found with this article online at http://dx.doi.org/10.1016/j.celrep.2014.08.044.

AUTHOR CONTRIBUTIONS

A.A. and A.T. designed and guided the research and wrote the manuscript. F.G. and M.P. contributed to research design. A.T., A.R., D.D.M., I.G., M.K., G.C., and C.M. conducted experiments. J.Z., R.G.-E., and C.V.C. performed and interpreted bioinformatics analysis. S.P. performed immunohistochemical experiments. M.S. and E.S. performed histopathological analysis on mouse samples. A.T., D.J., and D.D.M. performed FACS analysis.

ACKNOWLEDGMENTS

We thank all the members of the IRB animal core facility for technical assistance and the animal work. We thank Dr. Carole Pissot-Soldermann for developing NVP-BSK805. We thank Dr. Thomas Radimerski for providing NVP-BSK805 and advice on its use. We thank the P.P.P. laboratory for providing the *Pten* lox/lox mice and paraffin sections of murine invasive prostate cancer and all the members of the A.A. laboratory for the scientific discussions. This work was supported by Swiss National Science Foundation (SNSF) grant Ambizione (PZ00P3_136612/1), European Society for Medical Oncology (ESMO) translational research fellowship, Swiss Bridge Award, PEOPLE-IRG (22484), and European Research Council starting grant (ERCsg 261342) to A.A.; Empires donation to A.R.; and TRAIN Oncology fellowship to D.D.M.

Received: April 10, 2014
Revised: June 23, 2014
Accepted: August 20, 2014
Published: September 25, 2014

REFERENCES

Acharyya, S., Oskarsson, T., Vanharanta, S., Malladi, S., Kim, J., Morris, P.G., Manova-Todorova, K., Leversha, M., Hogg, N., Seshan, V.E., et al. (2012). A CXCL1 paracrine network links cancer chemoresistance and metastasis. Cell *150*, 165–178.

Acosta, J.C., Banito, A., Wuestefeld, T., Georgilis, A., Janich, P., Morton, J.P., Athineos, D., Kang, T.W., Lasitschka, F., Andrulis, M., et al. (2013). A complex secretory program orchestrated by the inflammasome controls paracrine senescence. Nat. Cell Biol. *15*, 978–990.

Akira, S. (2000). Roles of STAT3 defined by tissue-specific gene targeting. Oncogene *19*, 2607–2611.

Alimonti, A., Carracedo, A., Clohessy, J.G., Trotman, L.C., Nardella, C., Egia, A., Salmena, L., Sampieri, K., Haveman, W.J., Brogi, E., et al. (2010). Subtle variations in Pten dose determine cancer susceptibility. Nat. Genet. *42*, 454–458.

Alter, G., Malenfant, J.M., and Altfeld, M. (2004). CD107a as a functional marker for the identification of natural killer cell activity. J. Immunol. Methods *294*, 15–22.

Ansel, K.M., Harris, R.B., and Cyster, J.G. (2002). CXCL13 is required for B1 cell homing, natural antibody production, and body cavity immunity. Immunity *16*, 67–76.

Antonarakis, E.S., and Armstrong, A.J. (2011). Evolving standards in the treatment of docetaxel-refractory castration-resistant prostate cancer. Prostate Cancer Prostatic Dis. *14*, 192–205.

Antonarakis, E.S., Keizman, D., Zhang, Z., Gurel, B., Lotan, T.L., Hicks, J.L., Fedor, H.L., Carducci, M.A., De Marzo, A.M., and Eisenberger, M.A. (2012). An immunohistochemical signature comprising PTEN, MYC, and Ki67 predicts progression in prostate cancer patients receiving adjuvant docetaxel after prostatectomy. Cancer *118*, 6063–6071.

Baffert, F., Régnier, C.H., De Pover, A., Pissot-Soldermann, C., Tavares, G.A., Blasco, F., Brueggen, J., Chène, P., Drueckes, P., Erdmann, D., et al. (2010). Potent and selective inhibition of polycythemia by the quinoxaline JAK2 inhibitor NVP-BSK805. Mol. Cancer Ther. *9*, 1945–1955.

Bard-Chapeau, E.A., Li, S., Ding, J., Zhang, S.S., Zhu, H.H., Princen, F., Fang, D.D., Han, T., Bailly-Maitre, B., Poli, V., et al. (2011). Ptpn11/Shp2 acts as a tumor suppressor in hepatocellular carcinogenesis. Cancer Cell *19*, 629–639.

Braig, M., Lee, S., Loddenkemper, C., Rudolph, C., Peters, A.H., Schlegelberger, B., Stein, H., Dörken, B., Jenuwein, T., and Schmitt, C.A. (2005). Oncogene-induced senescence as an initial barrier in lymphoma development. Nature *436*, 660–665.

Chan, R.J., and Feng, G.S. (2007). PTPN11 is the first identified proto-oncogene that encodes a tyrosine phosphatase. Blood *109*, 862–867.

Chen, Z., Trotman, L.C., Shaffer, D., Lin, H.K., Dotan, Z.A., Niki, M., Koutcher, J.A., Scher, H.I., Ludwig, T., Gerald, W., et al. (2005). Crucial role of p53-dependent cellular senescence in suppression of Pten-deficient tumorigenesis. Nature *436*, 725–730.

Chien, Y., Scuoppo, C., Wang, X., Fang, X., Balgley, B., Bolden, J.E., Premsrirut, P., Luo, W., Chicas, A., Lee, C.S., et al. (2011). Control of the senescence-associated secretory phenotype by NF-κB promotes senescence and enhances chemosensitivity. Genes Dev. *25*, 2125–2136.

Collado, M. (2010). Exploring a 'pro-senescence' approach for prostate cancer therapy by targeting PTEN. Future Oncol. *6*, 687–689.

Collado, M., and Serrano, M. (2006). The power and the promise of oncogene-induced senescence markers. Nat. Rev. Cancer *6*, 472–476.

Coppé, J.P., Desprez, P.Y., Krtolica, A., and Campisi, J. (2010). The senescence-associated secretory phenotype: the dark side of tumor suppression. Annu. Rev. Pathol. *5*, 99–118.

Davalos, A.R., Coppe, J.P., Campisi, J., and Desprez, P.Y. (2010). Senescent cells as a source of inflammatory factors for tumor progression. Cancer Metastasis Rev. *29*, 273–283.

Deshmane, S.L., Kremlev, S., Amini, S., and Sawaya, B.E. (2009). Monocyte chemoattractant protein-1 (MCP-1): an overview. J. Interferon Cytokine Res. *29*, 313–326.

Dufour, J.H., Dziejman, M., Liu, M.T., Leung, J.H., Lane, T.E., and Luster, A.D. (2002). IFN-gamma-inducible protein 10 (IP-10; CXCL10)-deficient mice reveal a role for IP-10 in effector T cell generation and trafficking. J. Immunol. *168*, 3195–3204.

Gabrilovich, D.I., and Nagaraj, S. (2009). Myeloid-derived suppressor cells as regulators of the immune system. Nat. Rev. Immunol. *9*, 162–174.

Garnett, M.J., Edelman, E.J., Heidorn, S.J., Greenman, C.D., Dastur, A., Lau, K.W., Greninger, P., Thompson, I.R., Luo, X., Soares, J., et al. (2012). Systematic identification of genomic markers of drug sensitivity in cancer cells. Nature *483*, 570–575.

Glinsky, G.V., Glinskii, A.B., Stephenson, A.J., Hoffman, R.M., and Gerald, W.L. (2004). Gene expression profiling predicts clinical outcome of prostate cancer. J. Clin. Invest. *113*, 913–923.

Jackson, J.G., Pant, V., Li, Q., Chang, L.L., Quintás-Cardama, A., Garza, D., Tavana, O., Yang, P., Manshouri, T., Li, Y., et al. (2012). p53-mediated senescence impairs the apoptotic response to chemotherapy and clinical outcome in breast cancer. Cancer Cell *21*, 793–806.

Kang, T.W., Yevsa, T., Woller, N., Hoenicke, L., Wuestefeld, T., Dauch, D., Hohmeyer, A., Gereke, M., Rudalska, R., Potapova, A., et al. (2011). Senescence surveillance of pre-malignant hepatocytes limits liver cancer development. Nature *479*, 547–551.

Lukacs, R.U., Goldstein, A.S., Lawson, D.A., Cheng, D., and Witte, O.N. (2010). Isolation, cultivation and characterization of adult murine prostate stem cells. Nat. Protoc. *5*, 702–713.

Marotta, L.L., Almendro, V., Marusyk, A., Shipitsin, M., Schemme, J., Walker, S.R., Bloushtain-Qimron, N., Kim, J.J., Choudhury, S.A., Maruyama, R., et al. (2011). The JAK2/STAT3 signaling pathway is required for growth of $CD44^{+}CD24^{-}$ stem cell-like breast cancer cells in human tumors. J. Clin. Invest. *121*, 2723–2735.

Mombaerts, P., Iacomini, J., Johnson, R.S., Herrup, K., Tonegawa, S., and Papaioannou, V.E. (1992). RAG-1-deficient mice have no mature B and T lymphocytes. Cell *68*, 869–877.

Nardella, C., Clohessy, J.G., Alimonti, A., and Pandolfi, P.P. (2011). Pro-senescence therapy for cancer treatment. Nat. Rev. Cancer *11*, 503–511.

Ostrand-Rosenberg, S., and Sinha, P. (2009). Myeloid-derived suppressor cells: linking inflammation and cancer. J. Immunol. *182*, 4499–4506.

Parganas, E., Wang, D., Stravopodis, D., Topham, D.J., Marine, J.C., Teglund, S., Vanin, E.F., Bodner, S., Colamonici, O.R., van Deursen, J.M., et al. (1998). Jak2 is essential for signaling through a variety of cytokine receptors. Cell *93*, 385–395.

Pearson, H.B., Phesse, T.J., and Clarke, A.R. (2009). K-ras and Wnt signaling synergize to accelerate prostate tumorigenesis in the mouse. Cancer Res. *69*, 94–101.

Rodier, F., and Campisi, J. (2011). Four faces of cellular senescence. J. Cell Biol. *192*, 547–556.

Schlomm, T., Iwers, L., Kirstein, P., Jessen, B., Köllermann, J., Minner, S., Passow-Drolet, A., Mirlacher, M., Milde-Langosch, K., Graefen, M., et al. (2008). Clinical significance of p53 alterations in surgically treated prostate cancers. Mod. Pathol. *21*, 1371–1378.

Schwarze, S.R., Fu, V.X., Desotelle, J.A., Kenowski, M.L., and Jarrard, D.F. (2005). The identification of senescence-specific genes during the induction of senescence in prostate cancer cells. Neoplasia *7*, 816–823.

Setlur, S.R., Mertz, K.D., Hoshida, Y., Demichelis, F., Lupien, M., Perner, S., Sboner, A., Pawitan, Y., Andrén, O., Johnson, L.A., et al. (2008). Estrogen-dependent signaling in a molecularly distinct subclass of aggressive prostate cancer. J. Natl. Cancer Inst. *100*, 815–825.

Taylor, B.S., Schultz, N., Hieronymus, H., Gopalan, A., Xiao, Y., Carver, B.S., Arora, V.K., Kaushik, P., Cerami, E., Reva, B., et al. (2010). Integrative genomic profiling of human prostate cancer. Cancer Cell *18*, 11–22.

Trapani, J.A., and Sutton, V.R. (2003). Granzyme B: pro-apoptotic, antiviral and antitumor functions. Curr. Opin. Immunol. *15*, 533–543.

Trotman, L.C., Niki, M., Dotan, Z.A., Koutcher, J.A., Di Cristofano, A., Xiao, A., Khoo, A.S., Roy-Burman, P., Greenberg, N.M., Van Dyke, T., et al. (2003). Pten dose dictates cancer progression in the prostate. PLoS Biol. *1*, E59.

Tuveson, D.A., Shaw, A.T., Willis, N.A., Silver, D.P., Jackson, E.L., Chang, S., Mercer, K.L., Grochow, R., Hock, H., Crowley, D., et al. (2004). Endogenous oncogenic K-ras(G12D) stimulates proliferation and widespread neoplastic and developmental defects. Cancer Cell *5*, 375–387.

Vanneman, M., and Dranoff, G. (2012). Combining immunotherapy and targeted therapies in cancer treatment. Nat. Rev. Cancer *12*, 237–251.

Xue, W., Zender, L., Miething, C., Dickins, R.A., Hernando, E., Krizhanovsky, V., Cordon-Cardo, C., and Lowe, S.W. (2007). Senescence and tumour clearance is triggered by p53 restoration in murine liver carcinomas. Nature *445*, 656–660.

Yang, W., Wang, J., Moore, D.C., Liang, H., Dooner, M., Wu, Q., Terek, R., Chen, Q., Ehrlich, M.G., Quesenberry, P.J., and Neel, B.G. (2013). Ptpn11 deletion in a novel progenitor causes metachondromatosis by inducing hedgehog signalling. Nature *499*, 491–495.

Yu, H., Pardoll, D., and Jove, R. (2009). STATs in cancer inflammation and immunity: a leading role for STAT3. Nat. Rev. Cancer *9*, 798–809.

Zhu, X., Kong, D., Zhang, L., Sun, Y., Na, S., Han, C., and Jin, X. (2013). Correlation analysis of angiotensin-converting enzyme, angiotensinogen, and endothelial nitric oxide synthase gene polymorphisms and the progression of immunoglobulin A nephropathy/membranous nephropathy. Hum. Pathol. *44*, 2806–2813.

Zitvogel, L., Tesniere, A., Apetoh, L., Ghiringhelli, F., and Kroemer, G. (2008). [Immunological aspects of anticancer chemotherapy]. Bull. Acad Natl. Med. *192*, 1469–1487, discussion 1487–1489.

Cell Reports, Volume *9*

Supplemental Information

Enhancing Chemotherapy Efficacy in *Pten*-Deficient Prostate Tumors by Activating the Senescence-Associated Antitumor Immunity

Alberto Toso, Ajinkya Revandkar, Diletta Di Mitri, Ilaria Guccini, Michele Proietti, Manuela Sarti, Sandra Pinton, Jiangwen Zhang, Madhuri Kalathur, Gianluca Civenni, David Jarrossay, Erica Montani, Camilla Marini, Ramon Garcia-Escudero, Eugenio Scanziani, Fabio Grassi, Pier Paolo Pandolfi, Carlo V. Catapano, and Andrea Alimonti

Figure S1

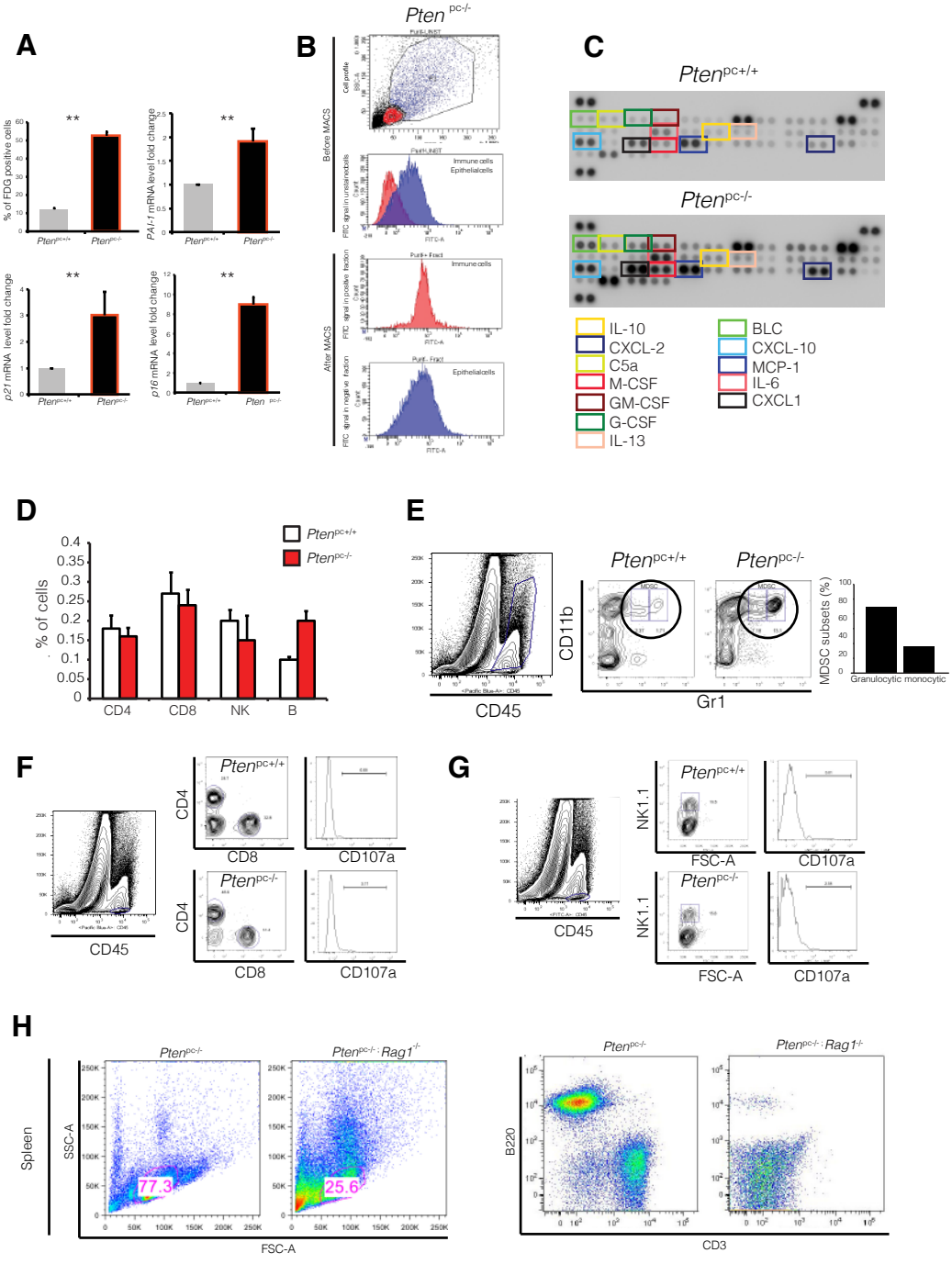
A
B
C
D
E
F
G
H
Pten pc-/-
Before MACS
After MACS
Immune cells
Epithelial cells
Ptenpc+/+
Ptenpc-/-
IL-10
CXCL-2
C5a
M-CSF
GM-CSF
G-CSF
IL-13
BLC
CXCL-10
MCP-1
IL-6
CXCL1
% of cells
CD4
CD8
NK
B
CD45
CD11b
Gr1
MDSC subsets (%)
Granulocytic
monocytic
CD107a
NK1.1
FSC-A
Spleen
SSC-A
77.3
25.6
Ptenpc-/-:Rag1-/-
B220
CD3

Figure S2

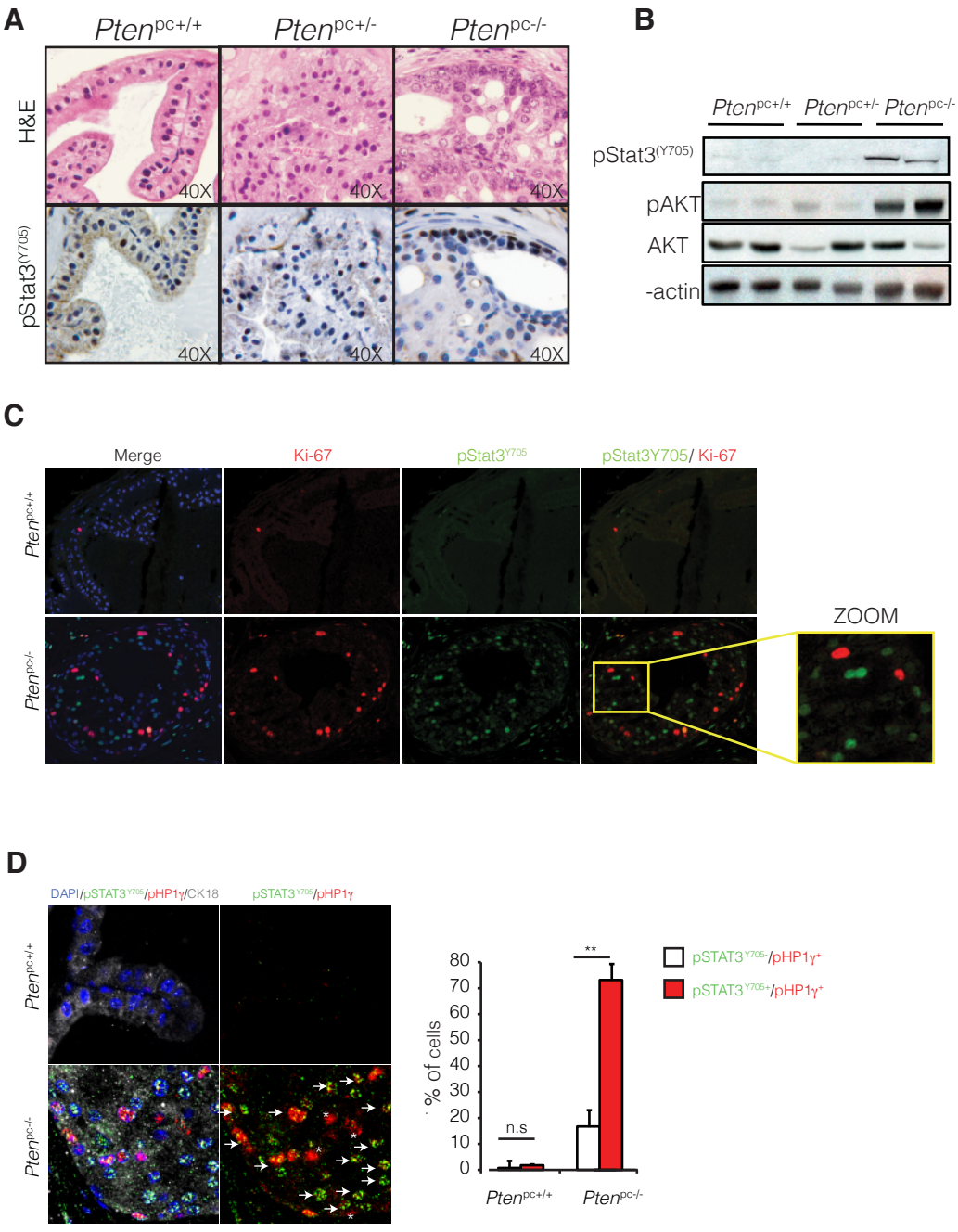
A
Pten pc+/+
Pten pc+/-
Pten pc-/-
H&E
pStat3 (Y705)
40X
B
Pten pc+/+
Pten pc+/-
Pten pc-/-
pStat3 (Y705)
pAKT
AKT
-actin
C
Merge
Ki-67
pStat3 Y705
pStat3Y705/ Ki-67
Pten pc+/+
Pten pc-/-
ZOOM
D
DAPI/pSTAT3 Y705/pHP1γ/CK18
pSTAT3 Y705/pHP1γ
Pten pc+/+
Pten pc-/-
% of cells
n.s
**
pSTAT3 Y705-/pHP1γ+
pSTAT3 Y705+/pHP1γ+

Figure S3

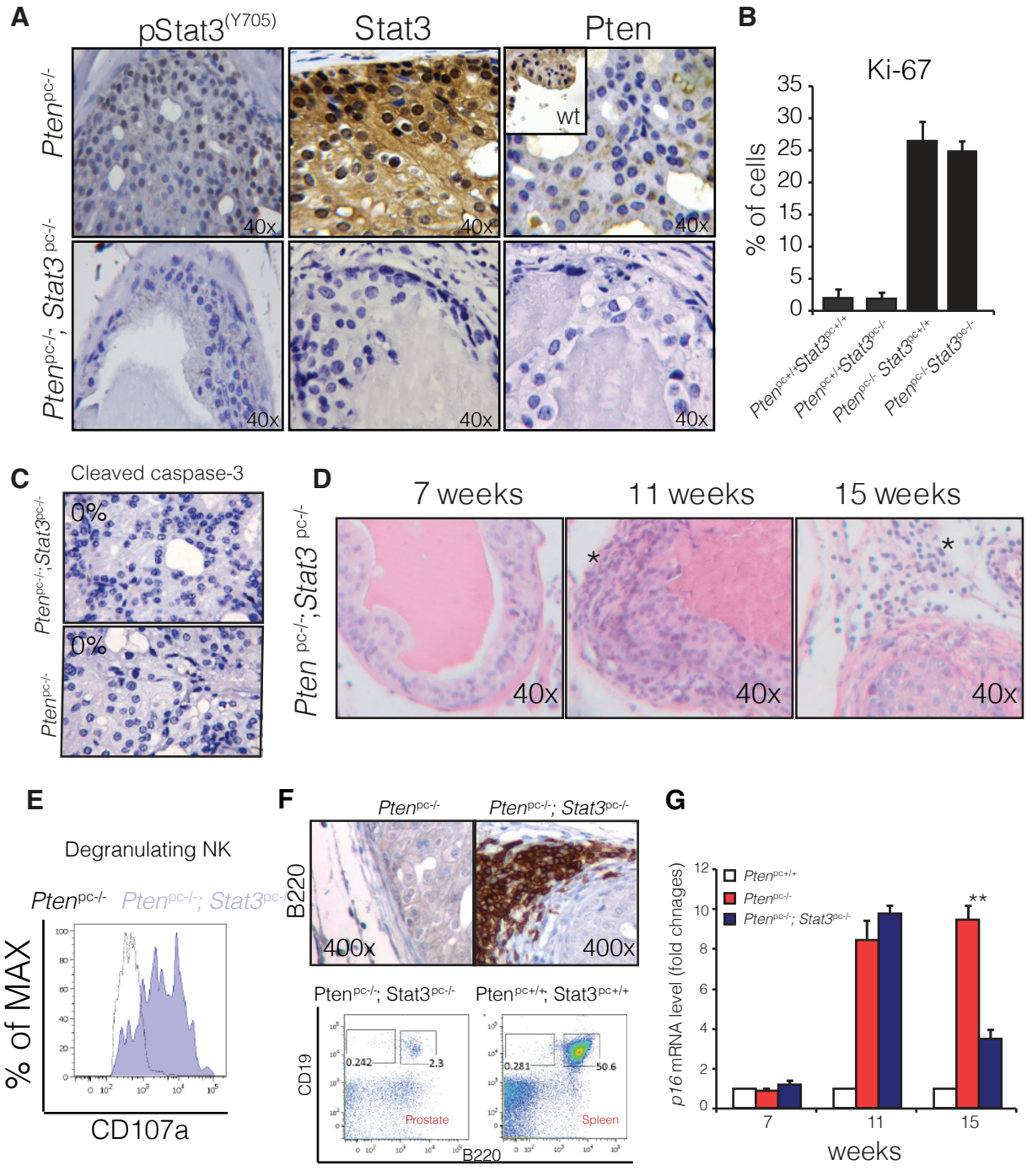
A
pStat3(Y705)
Stat3
Pten
Ptenpc-/-
Ptenpc-/-; Stat3 pc-/-
wt
40x
B
Ki-67
% of cells
35
30
25
20
15
10
5
0
Ptenpc+/+Stat3pc+/+
Ptenpc+/+Stat3pc-/-
Ptenpc-/- Stat3pc+/+
Ptenpc-/-Stat3pc-/-
C
Cleaved caspase-3
Ptenpc-/-;Stat3pc-/-
Ptenpc-/-
0%
D
7 weeks
11 weeks
15 weeks
Pten pc-/-;Stat3 pc-/-
*
40x
E
Degranulating NK
Ptenpc-/-
Ptenpc-/-; Stat3pc-/-
% of MAX
CD107a
F
Ptenpc-/-
Ptenpc-/-; Stat3pc-/-
B220
400x
Ptenpc-/-; Stat3pc-/-
Ptenpc+/+; Stat3pc+/+
CD19
0.242
2.3
Prostate
0.281
50.6
Spleen
B220
G
p16 mRNA level (fold chnages)
Ptenpc+/+
Ptenpc-/-
Ptenpc-/-; Stat3pc-/-
**
7
11
15
weeks

Figure S4

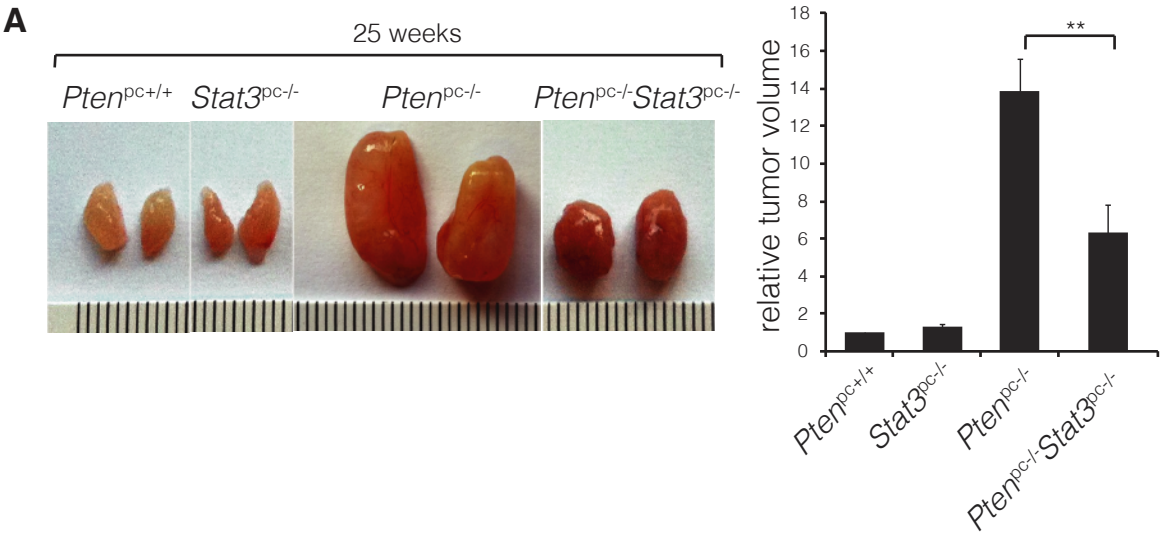
A
25 weeks
Pten pc+/+
Stat3 pc-/-
Pten pc-/-
Pten pc-/- Stat3 pc-/-
relative tumor volume
18
16
14
12
10
8
6
4
2
0
**
Pten pc+/+
Stat3 pc-/-
Pten pc-/-
Pten pc-/- Stat3 pc-/-

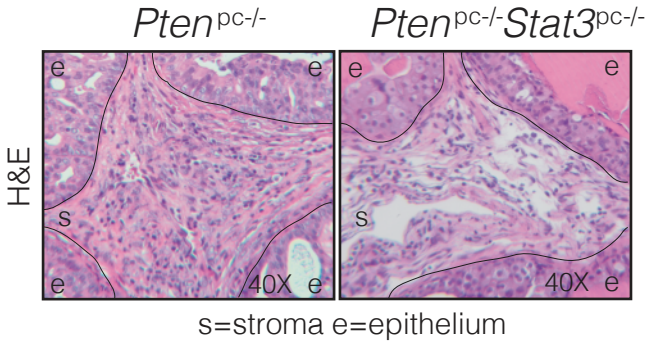
B
Pten pc-/-
Pten pc-/- Stat3 pc-/-
H&E
e
e
s
e
40X
e
e
e
s
40X
e
s=stroma e=epithelium

Figure S5

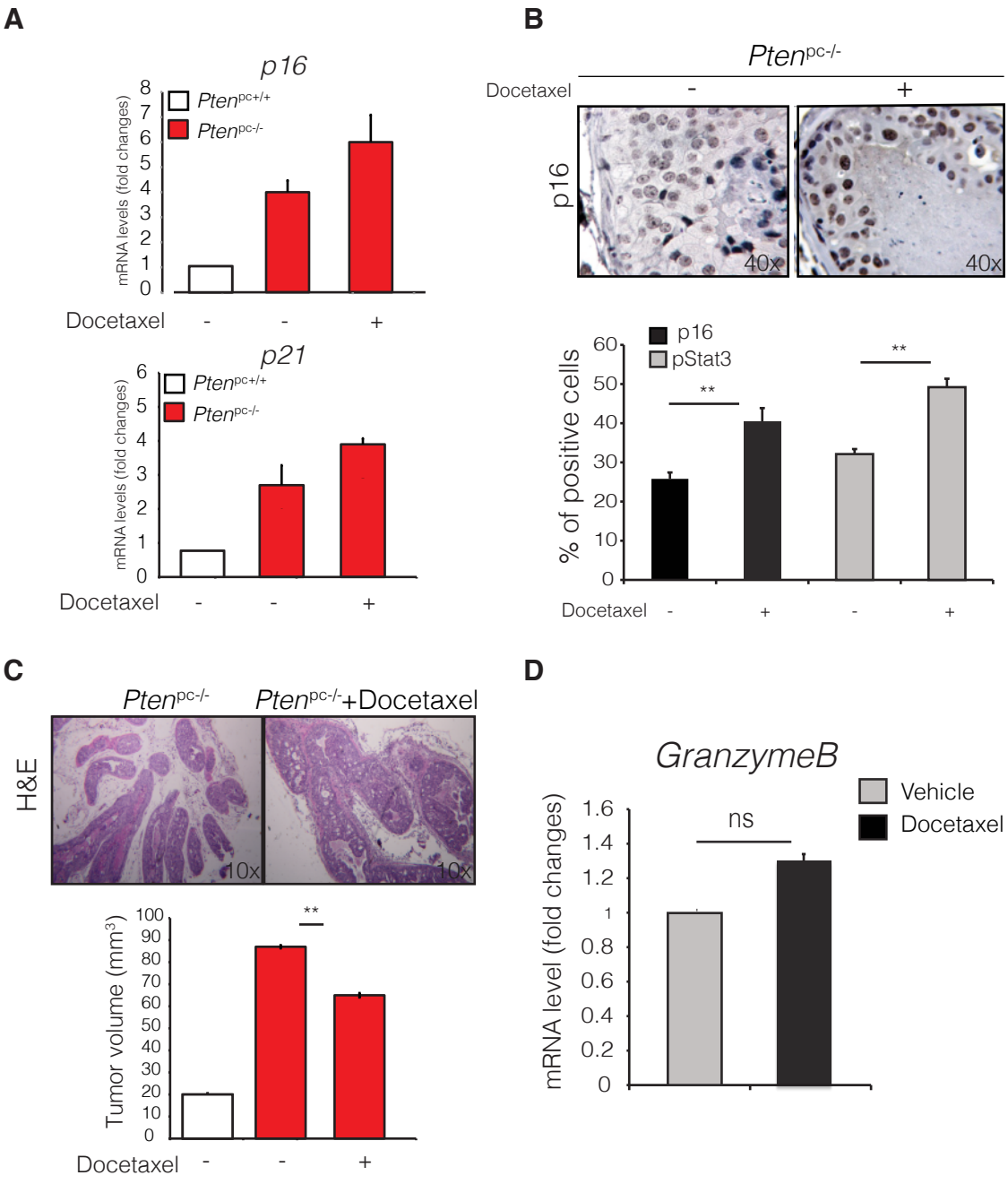
A
p16
Pten pc+/+
Pten pc-/-
mRNA levels (fold changes)
Docetaxel
p21
B
Pten pc-/-
Docetaxel
p16
40x
% of positive cells
p16
pStat3
**
C
Pten pc-/-
Pten pc-/-+Docetaxel
H&E
10x
Tumor volume (mm3)
D
GranzymeB
Vehicle
Docetaxel
ns
mRNA level (fold changes)

Figure S6

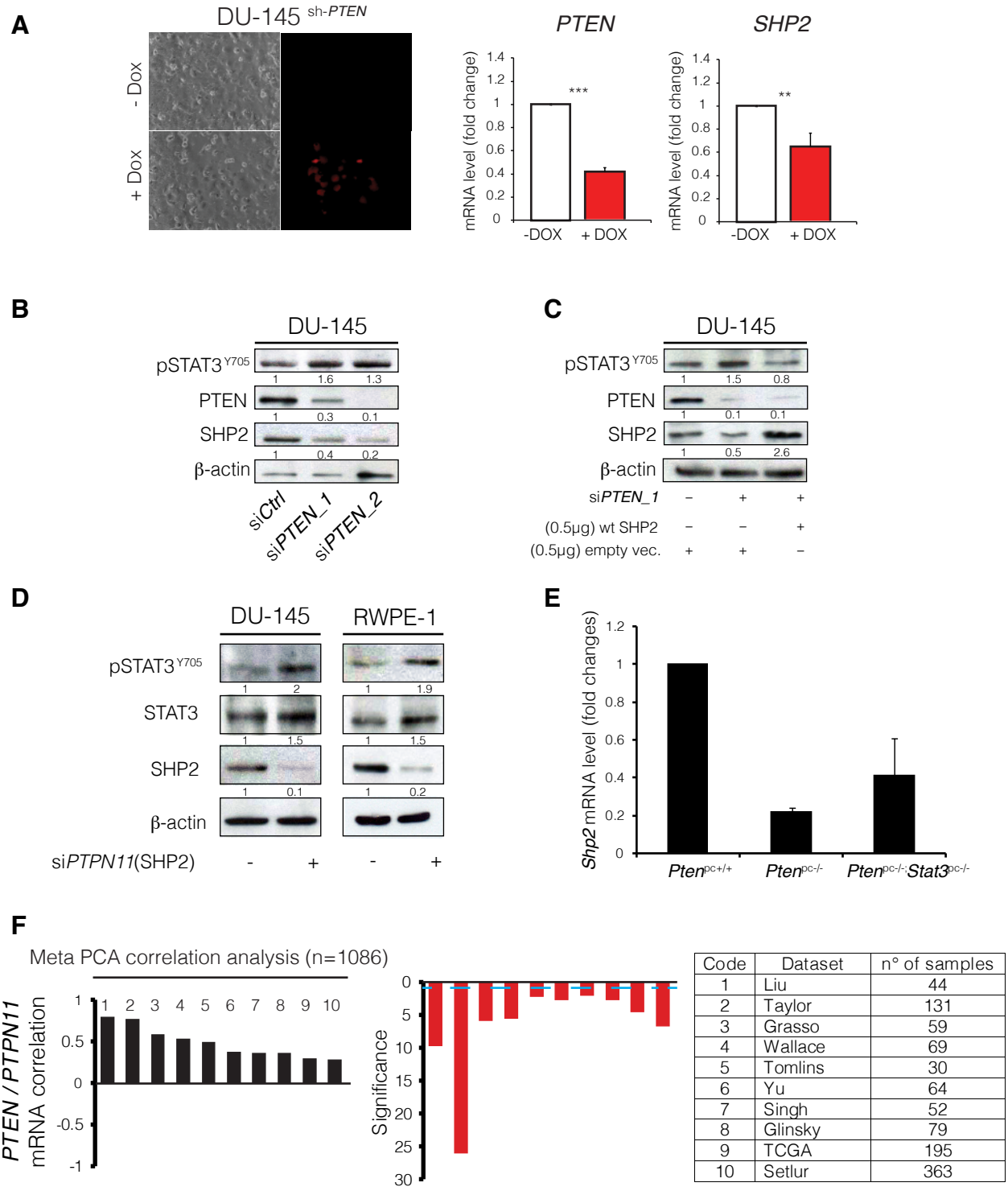

Code	Dataset	n° of samples
1	Liu	44
2	Taylor	131
3	Grasso	59
4	Wallace	69
5	Tomlins	30
6	Yu	64
7	Singh	52
8	Glinsky	79
9	TCGA	195
10	Setlur	363

Figure S7

A

	Type of Cancer	Correlation (pearson r)	Significance (p-val)
PTEN / PTPN11 significant correlation	PANCANCER (solid tissue normal=599)	0.57	7.0E-52
	PANCANCER (all=6609)	0.1	1.0E-17
	PANCANCER (primary tumor=5530)	0.07	0.00000010
	PANCANCER (primary blood derived cancer=173)	0.32	0.000020
	PANCANCER (metastatic=280)	0.19	0.0018
	PANCANCER (recurrent tumor=27)	0.05	0.78
	Thyroid Cancer (all=486)	0.44	2.00E-24
	Breast Cancer (all=991)	0.19	0.0000000034
	Acute Myeloid Leukemia (all=173)	0.32	0.000020
	Prostate Cancer (all=195)	0.29	0.000031
	Kidney Clear Cell Carcinoma (all=480)	0.18	0.000080
	Pancreatic Cancer (all=56)	0.47	0.00020
	Kidney Papillary Cell Carcinoma (all=141)	0.29	0.00050
	Lung Adenocarcinoma (all=468)	0.13	0.0038
	Endometrioid Cancer (all=118)	0.25	0.0069
	Melanoma (all=68)	0.29	0.017
	Kidney Chromophobe (all=66)	0.28	0.023
PTEN / PTPN11 not significant Correlation	Ovarian Cancer (all=262)	0.11	0.062
	Liver Cancer (all=134)	0.16	0.066
	Lower Grade Glioma (all=271)	0.11	0.077
	Bladder Cancer (all=182)	0.12	0.094
	Glioblastoma (all=154)	0.13	0.12
	Rectal Cancer (all=84)	0.13	0.22
	Sarcoma (all=75)	0.14	0.23
	Lung Squamous Cell Carcinoma (all=483)	-0.04	0.29
	Head and Neck Cancer (all=303)	0.058	0.32
	Cervical Cancer (all=145)	0.05	0.56
	Adrenocortical Cancer (all=79)	-0.06	0.60
	Colon Cancer (all=233)	0.02	0.71
	Uterine Carcinosarcoma (all=56)	0.04	0.73

B

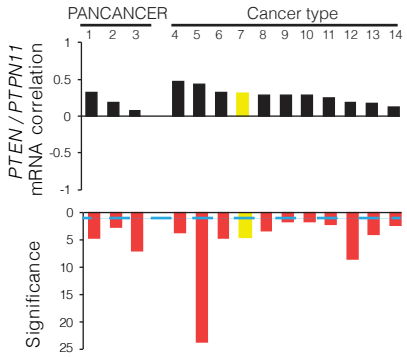

PTEN / PTPN11 significant correlation

Code	Cancer type	n° of samples
1	PANCER (primary blood derived cancer)	173
2	PANCER (metastatic)	280
3	PANCER (primary tumours)	5530
4	Pancreatic cancer	56
5	Thyroid cancer	486
6	Acute myeloid leukemia	173
7	Prostate cancer	195
8	Kidney papillary cell carcinoma	141
9	Melanoma	68
10	Kidney Chromophobe	66
11	Endometroid cancer	118
12	Breast cancer	991
13	Kidney clear cell carcinoma	480
14	Lung adenocarcinoma	468

C

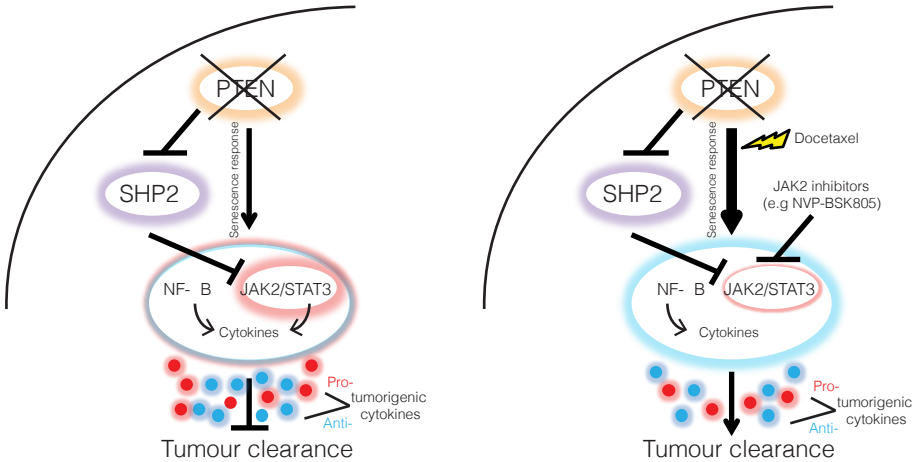

SUPPLEMENTAL FIGURE LEGENDS

Supplementary Figure S1, related to Figure 1. Efficiency of prostatic epithelial purification and immunophenotyping of *Pten*$^{pc-/-}$ senescent tumors (A) β-galactosidase activity (Fluorescein Di-β-D-galactopyranoside (FDG) positivity detected by FACS analysis) and mRNA levels of the senescence markers p16 (p=0.004), p21 (p=0.01) and PAI-1 (p=0.008) (n=4; **p<0.01). **(B)** Efficiency of purification obtained by magnetic cell sorting (MACS). Immune cells (CD45) , endothelial (CD31) and stromal (CD34) cells were stained in FITC and unstained epithelial cells were collected in the negative fraction with a purity >95%. **(C)** Cytokine array profiles in *Pten*$^{pc+/+}$ and *Pten*$^{pc-/-}$ prostates (n=3); colored squares indicates individual cytokines spotted in duplicate. **(D and E)** Strategy of gating used for the immunophenotyping of *Pten*$^{pc-/-}$ senescent tumors. Briefly, the immune cellular fraction in the tumor single cell suspension was identified by CD45 staining (pan- leukocyte marker) and different subpopulations were characterized as follow: **(D)** CD4 and CD8 staining (T cell), B220 (B cells) Nk1.1 staining (NK cells). **(E)** CD11b^{+}Gr1^{+} (MDSCs) subsets. Myeloid cells are marked in the circle. Monocytic MDSCs (CD11b^{hi}Gr1^{int}; left square) and granulocytic (CD11b^{hi}Gr1^{hi} ; right square) . **(F and G)** Degranulation of NK and CD8 cells was assessed by staining for the degranulation marker CD107a. **(H)** *Pten*$^{pc-/-}$; *Rag1*$^{-/-}$ mice lack B and T cells. SSC-A/FSC-A and CD3/B220 plots showing the genetic depletion of T and B cells in *Pten*$^{pc-/-}$; *Rag1*$^{-/-}$ mice. Spleen from a *Pten*$^{pc-/-}$ was used as a control. Data are represented as mean ± SEM.

Supplementary Figure S2, related to Figure 2. Stat3 activation in *Pten*$^{pc+/+}$, *Pten*$^{pc+/-}$ and *Pten*$^{pc-/-}$ tumors **(A)** H&E (upper panels) and pStat3$^{(Y705)}$ staining (lower panels) of *Pten*$^{pc+/+}$, *Pten*$^{pc+/-}$ and *Pten*$^{pc-/-}$ anterior prostates (APs). **(B)** Western blot analysis showing Stat3 phosphorylation in *Pten*$^{pc+/+}$, *Pten*$^{pc+/-}$ and *Pten*$^{pc-/-}$ APs. **(C)** Stat3 is activated in non proliferating cells in *Pten*$^{pc-/-}$ tumors. Confocal immunofluorescence images (IF) on *Pten*$^{pc+/+}$ and *Pten*$^{pc-/-}$ paraffin embedded APs tumor sections; in blue nuclear marker (DAPI), in red the proliferation marker (Ki67) and in green pStat3$^{(Y705)}$ positive cells. **(D**) Confocal immunofluorescence images (IF) on *Pten*$^{pc+/+}$ and *Pten*$^{pc-/-}$ paraffin embedded APs tumor sections; in blue nuclear marker (DAPI), in red the pHP1γ and in green pStat3$^{(Y705)}$ positive cells. Arrows indicate double positive cells. Data are represented as mean ± SEM.

Supplementary Figure S3, related to Figure 3. Phenotypic characterization of *Pten*$^{pc-/-}$; *Stat3*$^{pc-/-}$ tumors (A) Immunohistochemical analysis of Pten expression levels showed efficient deletion of Pten in both *Pten*$^{pc-/-}$ and *Pten*$^{pc-/-}$;*Stat3*$^{pc-/-}$ prostate tissues. Notably, immunohistochemical analysis shows enhanced expression of Stat3 in *Pten*$^{pc-/-}$ and efficient loss of Stat3 expression in *Pten*$^{pc-/-}$; *Stat3*$^{pc-/-}$ mouse models. **(B)** Bars represent the percentage of Ki-67 positive cells in APs of *Pten*$^{pc+/+}$; *Stat3*$^{pc+/+}$, *Pten*$^{pc+/+}$; *Stat3*$^{pc-/-}$, *Pten*$^{pc-/-}$; *Stat3*$^{pc+/+}$ and *Pten*$^{pc-/-}$; *Stat3*$^{pc-/-}$ 10 weeks old mice (n=3). **(C)** IHC showing absence of cleaved-caspase-3 staining in both *Pten*$^{pc-/-}$; *Stat3*$^{pc+/+}$ and *Pten*$^{pc-/-}$; *Stat3*$^{pc-/-}$ APs from 10 weeks old mice (n=3). **(D)** Progressive infiltration of immune cells in *Pten*$^{pc-/-}$; *Stat3*$^{pc-/-}$ tumors at different time points. **(E)** Histogram showing degranulation of NK cells in *Pten*$^{pc-/-}$; *Stat3*$^{pc-/-}$ tumors. **(F)** Representative images from *Pten*$^{pc-/-}$ and *Pten*$^{pc-/-}$; *Stat3*$^{pc-/-}$ sections stained for the B cell marker, B220 (400X) (upper panel) and FACS analysis revealing an enrichment of plasma cells ($CD19^{+}$ $B220^{-}$) in *Pten*$^{pc-/-}$; *Stat3*$^{pc-/-}$ tumors when compared to the normal levels present in spleen (lower panel). **(G)** p16 mRNA decay measured at different time points in tumors of different genotypes.

Supplementary Figure S4, related to Figure 3. Phenotypic characterization of *Pten*$^{pc-/-}$; *Stat3*$^{pc-/-}$ tumors at late stage (A) Representative images and size of APs from 25 weeks old mice (n=4, $^{**}p<0.01$). **(B)** H&E staining showing the reduced stroma in *Pten*$^{pc-/-}$; *Stat3*$^{pc-/-}$ tumors of 25 weeks old mice.

Supplementary Figure S5, related to Figure 4. Docetaxel is poorly effective in *Pten*$^{pc-/-}$ tumors (A) p16 and p21 mRNA levels in *Pten*$^{pc-/-}$ tumors untreated and treated with Docetaxel. **(B)** (Upper panel) p16 staining in *Pten*$^{pc-/-}$ tumors untreated and treated with Docetaxel. (Lower panel) Quantification of p16 and pStat3$^{(Y705)}$ in tumor untreated and treated with Docetaxel (n=3; **p<0.01). **(C)** H&E staining (upper panel) and tumor volume (n=3; **p<0.01) (lower panel) of *Pten*$^{pc-/-}$ tumors untreated and treated with Docetaxel. **(D)** *GranzymeB* mRNA levels in *Pten*$^{pc-/-}$ tumors treated with vehicle and Docetaxel (ns= not significant). Data are represented as mean ± SEM.

Supplementary Figure S6, related to Figure 6. Correlation between *PTEN/PTPN11* levels in mouse and human PCA (A) DU-145 prostate cells stably infected with a Doxycycline (Dox) RFP-labeled inducible ShRNA designed against *PTEN* (upper panel). mRNA levels of *PTEN* and *SHP2* in DU-145^{shPTEN} prostate cell line after Dox treatment (lower panel). **(B)** DU-145 cells transfected with two different si*PTEN*

for 72hrs. **(C)** DU-145 cells co-transfected with an si*PTEN* and a plasmid expressing wt-SHP2 for 72hrs **(D)** DU-145 and RWPE-1 cell lines transfected with si*PTPN11* for 72hrs. **(E)** *Shp2* mRNA levels in $Pten^{pc-/-}$; $Stat3^{pc-/-}$ mice. **(F)** Gene expression levels for *PTEN* and *PTPN11* was analyzed using pearson correlation test (see material and methods) in 10 human prostate cancer datasets. Upper bar plots indicate pearson "r" correlation values. Bottom bar plots indicates significance of pearson correlations as $-\log_{10}$(p-val) values. Blue line corresponds to p-val=0.05, meaning that bars spanning above the line are significant. All 10 datasets display significant co-expression between *PTEN* and *PTPN11*. Numbers on top of the bars indicate a specific dataset, listed in the table (bottom right).

Supplementary Figure S7, related to Figure 7. *PTEN-PTPN11* correlation in PANCANCER analysis and model (A) Table shows r values and p-values, per type of sample and cancer cohort (green= *PTEN-PTPN11* correlation is significant ; red= *PTEN-PTPN11* correlation is NOT significant). **(B)** Tumor cohorts with significant correlations are shown. Upper bar plots indicate pearson "r" correlation values. Bottom bar plots indicate significance of pearson correlations as $-\log_{10}$(p-val) values. Blue line corresponds to p-val=0.05, meaning that bars spanning above the line are significant (p-val<0.05). Numbers on top of the bars indicate a specific dataset, listed in the table. Prostate cancer is highlighted in yellow. Importantly, all significant associations are positive (r >0). **(C)** Model. PICS is characterized by an immunosuppressive SASP shaped by the activation of both Nf-kB and STAT3. Loss of PTEN induces down-regulation of SHP2 a negative regulator of the JAK2/STAT3 pathway. Our genetic evidence revealed that STAT3 orchestrates the immunosuppressive feature of the SASP by tilting the balance between pro- and anti-tumorigenic cytokines in the tumor microenvironment in favor of the pro-tumorigenic cytokines (left panel). Treatment of *PTEN* null tumors with Docetaxel boosts the senescence response but fails to induce an anti-tumor immune response. However, when *PTEN* null tumors are treated with Docetaxel in combination with a JAK2 inhibitor the SASP is reprogrammed (R-SASP) and the level of pro-tumorigenic cytokines are reduced favoring anti-tumor immune response (right panel).